

Mesoscale Modeling of Springtime Arctic Mixed-Phase Stratiform Clouds Using a New Two-Moment Bulk Microphysics Scheme

H. MORRISON

Department of Aerospace Engineering, University of Colorado, Boulder, Colorado

J. O. PINTO

Department of Aerospace Engineering, University of Colorado, and National Center for Atmospheric Research, Boulder, Colorado

(Manuscript received 4 October 2004, in final form 13 March 2005)

ABSTRACT

A new two-moment bulk microphysics scheme is implemented into the polar version of the fifth-generation Pennsylvania State University–NCAR Mesoscale Model (MM5) to simulate arctic mixed-phase boundary layer stratiform clouds observed during Surface Heat Budget of the Arctic (SHEBA) First International Satellite Cloud Climatology Project (ISCCP) Regional Experiment (FIRE) Arctic Cloud Experiment (ACE). The microphysics scheme predicts the number concentrations and mixing ratios of four hydrometeor species (cloud droplets, small ice, rain, snow) and includes detailed treatments of droplet activation and ice nucleation from a prescribed distribution of aerosol obtained from observations. The model is able to reproduce many features of the observed mixed-phase cloud, including a near-adiabatic liquid water content profile located near the top of a well-mixed boundary layer, droplet number concentrations of about $200\text{--}250\text{ cm}^{-3}$ that were distributed fairly uniformly through the depth of the cloud, and continuous light snow falling from the cloud base to the surface. The impacts of droplet and ice nucleation, radiative transfer, turbulence, large-scale dynamics, and vertical resolution on the simulated mixed-phase stratiform cloud are examined. The cloud layer is largely self-maintained through strong cloud-top radiative cooling that exceeds 40 K day^{-1} . It persists through extended periods of downward large-scale motion that tend to thin the layer and reduce water contents. Droplet activation rates are highest near cloud base, associated with subgrid vertical motion that is diagnosed from the predicted turbulence kinetic energy. A sensitivity test neglecting subgrid vertical velocity produces only weak activation and small droplet number concentrations ($<90\text{ cm}^{-3}$). These results highlight the importance of parameterizing the impact of subgrid vertical velocity to generate local supersaturation for aerosol-droplet closure. The primary ice nucleation mode in the simulated mixed-phase cloud is contact freezing of droplets. Sensitivity tests indicate that the assumed number and size of contact nuclei can have a large impact on the evolution and characteristics of mixed-phase cloud, especially the partitioning of condensate between droplets and ice.

1. Introduction

With increased computing power, physical parameterizations in atmospheric models have become more sophisticated. Many climate and numerical weather prediction (NWP) models now incorporate fairly detailed bulk cloud microphysics parameterizations. These schemes predict the mass or mixing ratio of one or more cloud water/precipitation species and represent

the size spectra with a distribution function (e.g., Lin et al. 1983; Rutledge and Hobbs 1984; Dudhia 1989; Walko et al. 1995; Reisner et al. 1998; Kong and Yau 1997). A recent improvement in bulk schemes has been the prediction of two moments of the hydrometeor size spectra, that is, the number concentration and mass/mixing ratio of the species (e.g., Levkov et al. 1992; Ferrier 1994; Harrington et al. 1995; Meyers et al. 1997; Girard and Curry 2001; Morrison et al. 2005a, hereafter M05a), increasing the degrees of freedom associated with the particle spectra and improving calculations of the microphysical processes and radiative transfer (Meyers et al. 1997). Droplet and crystal concentrations are important since they influence particle size, and

Corresponding author address: Dr. Hugh Morrison, Dept. of Aerospace Engineering, University of Colorado, Boulder, CO 80309.

E-mail: hugh@cloud.colorado.edu

hence sedimentation, collision/accretion, and cloud radiative properties (e.g., Twomey 1977; Albrecht 1989; Stevens et al. 1996; Ghan et al. 1997; DeMott et al. 1997; Lohmann et al. 2001; Jensen et al. 2004).

Droplet and ice crystal concentrations and sizes are particularly important in supercooled arctic clouds (e.g., Hobbs and Rangno 1998; Rangno and Hobbs 2001; Pinto 1998; Pinto et al. 2001; Harrington et al. 1999). Rangno and Hobbs (2001) found that arctic clouds with a maximum droplet effective radius greater than 12 μm (generally associated with droplet number concentrations less than 100 cm^{-3}) at temperature between -4° and -10°C often contained ice, while clouds with a smaller maximum effective radius (associated with larger droplet number concentrations) tended to be ice free. The ice crystal concentration is important in supercooled clouds since it determines in part the time scale governing the uptake of water vapor by depositional growth of the crystals (i.e., the supersaturation relaxation time scale). When the ice concentration is high, supersaturation relaxation is often short and the uptake of water vapor occurs quickly. This enhanced Bergeron–Findeisen process (i.e., transfer of water vapor from droplets to crystals) has been implicated in the rapid glaciation of arctic mixed-phase stratiform clouds (MPS; Hobbs and Rangno 1998; Pinto 1998). Rauber and Tokay (1991) hypothesized that liquid water was maintained at the top of orographic MPS because of the occurrence of small crystals, since small crystals limit the uptake of water vapor and hence weaken the Bergeron process. Modeling studies of arctic MPS have exhibited large sensitivities to the specified ice particle or ice nuclei (IN) number concentrations (Harrington et al. 1999; Jiang et al. 2000; Morrison et al. 2003; Morrison et al. 2005b). The often poor simulation of arctic MPS in climate and NWP models has been attributed to uncertainties in the modeled droplet and ice crystal concentrations (Girard and Curry 2001; Morrison et al. 2003; Morrison et al. 2005b).

Further motivation for the detailed treatment of cloud particle number concentrations and nucleation processes in models is the hypothesis that anthropogenic aerosol influences the microphysical and radiative properties of clouds (e.g., Twomey 1977; Albrecht 1989). Droplet and crystal concentrations are related to the number of cloud condensation nuclei (CCN) and IN available, which are a function of the local aerosol characteristics. Hence, modification of the aerosol is expected to significantly influence the cloud particle number concentration. Most studies have focused on aerosol modification of the droplet population (e.g., Albrecht 1989; Coakley and Walsh 2002; Ghan et al. 2001; Rotsteyn and Penner 2001; Feingold et al. 2003),

but aerosol–ice interactions may also have a significant impact on ice- and mixed-phase clouds (e.g., DeMott et al. 1997; Lohmann et al. 2001; Lohmann 2002a,b; Morrison et al. 2005b). The properties of arctic MPS may be particularly susceptible to changes in the aerosol characteristics (Curry 1995; Curry et al. 1996; Morrison et al. 2005b). This sensitivity is climatically important since MPS dominate the radiative forcing at the surface of the Arctic during much of the year (Intrieri et al. 2002; Shupe and Intrieri 2004; Zuidema et al. 2005, hereafter Z05).

A fundamental question remains as to whether increasing sophistication of the parameterized microphysics, including the prediction of nucleation processes and particle number concentrations, is necessarily suitable for large-scale models, since cloud processes in reality occur over scales that often cannot be resolved. Detailed treatments of droplet and/or crystal number concentrations, including the nucleation processes, have been incorporated into a number of climate and NWP models (e.g., Ghan et al. 1997; Meyers et al. 1997; Lohmann et al. 2001; Levkov et al. 1992; Ferrier 1994). However, the role of nucleation and particle number concentrations in arctic MPS is highly uncertain (e.g., Curry et al. 1996; Curry et al. 2000; Pinto 1998; Jiang et al. 2000). Furthermore, these models have not been extensively tested against observations in terms of their ability to simulate arctic MPS. The correct prediction of arctic MPS is especially important since these clouds have a large impact on the surface radiative fluxes and sea ice melting rates (Curry et al. 1993; Intrieri et al. 2002; Shupe and Intrieri 2004; Z05).

To address these concerns, we incorporate a new two-moment bulk microphysics scheme (M05a) into the polar version of the fifth-generation Pennsylvania State University (PSU)–National Center for Atmospheric Research (NCAR) Mesoscale Model (MM5; Bromwich et al. 2001) to simulate a MPS deck observed on 4–5 May 1998, during the Surface Heat Budget of the Arctic Ocean (SHEBA) project and First International Satellite Cloud Climatology Project (ISCCP) Regional Experiment Arctic Clouds Experiment (FIRE ACE). The microphysics scheme incorporates a physically based treatment of droplet and crystal number concentrations, including detailed parameterizations of ice nucleation and droplet activation from a specified aerosol distribution (obtained from observations). This allows for the simulation of cloud–aerosol interactions in liquid-, mixed-, and ice-phase clouds. The subgrid-scale dynamics driving the microphysics are parameterized in terms of the predicted turbulence kinetic energy (TKE). Model output is compared to detailed in situ cloud microphysical observations and retrievals ob-

tained from remotely based sensors, and key model parameters involved in the prediction of MPS are examined. The text is organized as follows: section 2 describes the instrumentation and retrieval techniques. Section 3 provides a brief description of the microphysics scheme. The MM5 configuration and model forcing is outlined in section 4. A brief description of the case study is given in section 5. The results are presented in section 6 and sensitivity tests investigating the formation and dissipation of MPS are detailed in section 7. Summary and conclusions are given in section 8.

2. Observations

SHEBA is described in detail by Uttal et al. (2002). A heavily instrumented icebreaker ship was frozen into the multiyear sea ice on 1 October 1997 at 75.27°N, 142.68°W, and allowed to drift for 1 yr across the Beaufort and Chukchi Seas. FIRE ACE was conducted in coordination with SHEBA and used aircraft to measure in situ cloud and aerosol characteristics near the SHEBA site (Curry et al. 2000).

Temperature and relative humidity profiles at SHEBA were measured by rawinsondes launched 4 times per day. Surface and near-surface meteorological conditions were obtained from tower measurements (Persson et al. 2002). Cloud properties were retrieved from a collection of ground-based instruments deployed at SHEBA. A vertically pointing, 35-GHz, millimeter cloud radar (MMCR) made continuous measurements of reflectivity and mean Doppler velocity up to a height of 13 km. Collocated with the MMCR were a dual-channel microwave radiometer (MWR) and a depolarization micropulse lidar used to remotely determine liquid water path (LWP), cloud phase, and cloud-base height (Westwater et al. 2001; Intrieri et al. 2002). Retrieval techniques for estimating the ice water contents are described in Shupe et al. (2001). Relative uncertainty for the retrieved ice water content (IWC) is 60%–70% (Shupe et al. 2001). LWPs were retrieved from the MWR brightness temperatures (Han and Westwater 1995) using dry opacity and cloud liquid absorption models of Rosenkranz (1998) and Liebe et al. (1991). Uncertainty in the MWR-derived LWP is 10 g m^{-2} (Z05). Radar retrievals of liquid water content (LWC) profiles were not performed for mixed-phase clouds since ice tends to dominate the radar signal. Estimates of LWC have been made by assuming adiabatic ascent of a parcel from the lidar-determined cloud base and constraining the column-integrated values to the MWR-derived LWP (Z05). Comparisons with in situ aircraft data validate this multisensor/adiabatic approach for determining the LWC (Z05). Hereafter, the con-

strained adiabatic LWC will be referred to as the retrieved LWC. Note that retrievals may smooth sharp transitions in cloud structure, particularly in the vertical.

In situ cloud and aerosol microphysical properties were obtained from an array of instruments flown on the NCAR C-130Q as part of FIRE ACE. These instruments are detailed in Curry et al. (2000), Lawson et al. (2001), Z05, Yum and Hudson (2001), and Rogers et al. (2001). LWC was determined by the mean of two King hotwire probes located on each side of the aircraft (the values were generally within 10% of each other). Droplet number concentration and effective radius were determined from a Forward Scattering Spectrometer (FSSP) probe (Z05). The FSSP consistently overestimates the LWC in mixed-phase clouds (Lawson et al. 2001), but is more prone to error in drop sizing than counting (Lawson 2003). The FSSP LWC is scaled for consistency with the King probe data. The droplet effective radius is determined by the FSSP droplet number concentration and size distribution dispersion and scaled FSSP LWC. Since the number concentration of ice particles is much smaller (about four orders of magnitude) than the droplet concentration for this case, we assume that in liquid containing regions the FSSP data correspond completely to liquid particles. Similarly, we assume that residual ice collection on the King probe is negligible. Ice crystal concentration and IWC were determined from combined FSSP, 260X 1D Optical Array Probe, and CPI measurements (Lawson et al. 2001; Lawson 2003; Z05). The IN concentrations were obtained from a continuous flow diffusion chamber (Rogers et al. 2001). Condensation nuclei (CN) and CCN concentrations were measured with a TSI 3010 CN counter and Desert Research Institute CCN spectrometer, respectively (Yum and Hudson 2001).

Five-kilometer data from the Advanced Very High Resolution Radiometer Polar Pathfinder Project were analyzed to provide retrievals of cloud properties over the Arctic during SHEBA FIRE ACE (Maslanik et al. 2001). Pathfinder data products are twice-daily composites of AVHRR images centered on 0400 and 1400 local solar time (~ 1500 and 0100 UTC). Acquisition times for a given pixel may have varied several hours from this time. Cloud properties were retrieved using algorithms of the Cloud and Surface Parameter System described by Key (2001). The satellite products agree well with in situ observations and ground-based retrievals obtained during SHEBA FIRE ACE (Maslanik et al. 2001).

3. Description of the microphysics scheme

The two-moment microphysics scheme described by M05a predicts the number concentration, N , and mix-

ing ratio, q , of four hydrometeor species: droplets, cloud ice, snow, and rain. The hydrometeor size distributions are represented by gamma functions. The microphysical processes in the scheme represent the source/sink terms for N and q in the kinetic equations. The kinetic equations for N and q depend on space variables x , y , and z and time t , that is, $N = N(x, y, z, t)$

$$\begin{aligned} \frac{\partial q}{\partial t} = & -\nabla \cdot (\mathbf{v}q) + \frac{\partial}{\partial z} (V_{qx}) + \nabla_D q + \left(\frac{\partial q}{\partial t}\right)_{\text{PRO}} \\ & + \left(\frac{\partial q}{\partial t}\right)_{\text{COND/DEP}} + \left(\frac{\partial q}{\partial t}\right)_{\text{AUTO}} \\ & + \left(\frac{\partial q}{\partial t}\right)_{\text{COAG}} + \left(\frac{\partial q}{\partial t}\right)_{\text{MLT/FRZ}} \\ & + \left(\frac{\partial q}{\partial t}\right)_{\text{MULT}} \end{aligned} \quad (1)$$

$$\begin{aligned} \frac{\partial N}{\partial t} = & -\nabla \cdot (\mathbf{v}N) + \frac{\partial}{\partial z} (V_{Nx}) + \nabla_D N + \left(\frac{\partial N}{\partial t}\right)_{\text{PRO}} \\ & + \left(\frac{\partial N}{\partial t}\right)_{\text{EVAP/SUB}} + \left(\frac{\partial N}{\partial t}\right)_{\text{AUTO}} \\ & + \left(\frac{\partial N}{\partial t}\right)_{\text{SELF}} + \left(\frac{\partial N}{\partial t}\right)_{\text{COAG}} \\ & + \left(\frac{\partial N}{\partial t}\right)_{\text{MLT/FRZ}} + \left(\frac{\partial N}{\partial t}\right)_{\text{MULT}}, \end{aligned} \quad (2)$$

where \mathbf{v} is the 3D wind vector, and V_{Nx} and V_{qx} denote the number-weighted and mass-weighted terminal particle fall speed for each species. Here, ∇_D is the turbulent diffusion operator. The first three terms of the right-hand side of (1) and (2) involve spatial derivatives: advection, sedimentation, and turbulent diffusion. The remainder of the terms on the right-hand side of (1) and (2) are the microphysical processes. The last six terms in (1) are the following: primary production (ice nucleation or droplet activation), condensation/deposition (evaporation/sublimation), autoconversion (parameterized transfer of mass and number concentration from the cloud ice and droplet classes to snow and rain due to coalescence and diffusional growth), collection between hydrometeor species, melting/freezing, and ice multiplication (transfer of mass from the snow class to ice). The last seven terms in (2) are the following: primary production, evaporation/sublimation, autoconversion, self-collection, collection between hydrometeor species, melting/freezing, and ice multiplication. A detailed description of the microphysical processes is given by M05a. The microphysics parameters are described in M05a except as discussed below. Since we particularly focus on how droplet and crystal nucle-

ation impact the MPS, these parameterizations are described here in more detail.

a. Droplet activation

Droplet activation is calculated by applying Kohler theory to a Junge distribution of dry aerosol following Khvorostyanov and Curry (1999a), where the dry aerosol size distribution is given by

$$f_a(r_D) = N_a(\mu - 1)r_{\min}^{\mu-1}r_D^{-\mu}, \quad (3)$$

where r_D is the dry aerosol radius, N_a is the total number concentration, r_{\min} is the mode, and μ is the slope of the dry aerosol size distribution. The parameter r_{\min} provides a nonzero modal value for aerosol size spectrum, thereby preventing an unbounded number concentration at zero radius. Applying Kohler theory to (3) (see Khvorostyanov and Curry 1999a) the potential number of aerosols activated (N') at a given supersaturation, S , (i.e., CCN activity spectrum) is given by

$$N' = \min(C_T S^k, N_a), \quad (4)$$

where C_T and k are defined in Khvorostyanov and Curry (1999a) as a function of the aerosol parameters in (3) (e.g., N_a , r_{\min} , μ) and the aerosol chemical composition and soluble fraction. Here, the aerosol parameters are specified so that the CCN activity spectra calculated by (4) match with observed CCN spectra obtained during FIRE ACE (see section 4).

Observed vertical velocity spectra in arctic MPS indicate that most kinetic energy is associated with eddies less than 1 km in size (Pinto 1998), implying that large-scale models will not be able to resolve the vertical motion leading to droplet activation. Thus, we parameterize the subgrid vertical velocity as a function of the predicted TKE for calculations of droplet activation similar to the approach developed by Ghan et al. (1997). Given the relationship between vertical velocity variance and TKE expressed as (Stull 1988)

$$\text{TKE} = \frac{1}{2}(u'^2 + v'^2 + w'^2), \quad (5)$$

and assuming that $w' = u' = v'$ as found by Pinto (1998) in low-level arctic MPS, a characteristic subgrid vertical velocity w' is diagnosed from the TKE predicted by the model (see section 4)

$$w' = \left(\frac{2}{3} \text{TKE}\right)^{(1/2)}. \quad (6)$$

We note that other processes can produce subgrid vertical motion (e.g., gravity waves, orography; Ghan et al. 1997) but only consider turbulence here.

For an activity spectrum of the form (4) consistent

with the Twomey (1959) formulation, the potential number of aerosols activated is given by Rogers and Yau (1989)

$$N' = \min[0.88C_T^{2(k+2)}(0.07w_{\text{ef}}^{3/2})^{k/(k+2)}, N_a], \quad (7)$$

where N' is in cm^{-3} and w_{ef} is the effective vertical velocity in cm s^{-1} . The term w_{ef} takes into account the grid-scale and subgrid vertical velocity and diabatic heating due to radiative transfer following Khvorostyanov and Curry (1999b). Since turbulence may be underpredicted, particularly if the vertical resolution is poor, a minimum value of 10 cm s^{-1} is specified for w_{ef} following Ghan et al. (1997).

The parameter N' represents the potential number of activated aerosols; the actual activation rate (NCN) depends upon the existing number of cloud droplets,

$$\text{NCN} = \max\left(\frac{N' - N_c}{2\Delta t}, 0\right), \quad (8)$$

where Δt is the model time step and N_c is the number concentration of existing droplets. The factor of 2 accounts for the fact that both upward and downward subgrid vertical velocities are present within the grid cell, while only upward vertical velocities promote droplet activation.

Since prognostic aerosol is not considered in the present version of the scheme, changes in the aerosol size and chemical composition due to cloud–aerosol interactions are neglected. As pointed out by Feingold et al. (1999), these variations may have significant impact on the number of aerosols activated under certain circumstances. An additional simplifying assumption is made by using a single characteristic subgrid vertical velocity calculated for each level rather than a distribution of w' as occurs in the real atmosphere. This assumption is a potential source of bias since the relationship between N' and w_{ef} is generally nonlinear. On the other hand, numerical integration of (7) using a distribution of w' is computationally expensive and the distribution of w' in the real atmosphere is uncertain. Additional work is needed to determine how to best parameterize the distribution of w' in the atmosphere and its influence on droplet activation.

M05a found that reduction of N_c because of evaporation had little impact on the simulation, similar to results reported by Ghan et al. (1997). However, here we use a vertical grid spacing and time step much smaller than was used in the studies above, and find that changes in N_c due to evaporation can impact profiles of droplet concentration. Here, the loss of N_c during evaporation is parameterized in terms of the change

in q_c , such that the relative loss of number is equal to the relative loss of mixing ratio. We note that this parameterization is uncertain and should be further tested and developed (e.g., by comparison with bin microphysics schemes).

b. Homogeneous and heterogeneous ice nucleation

At temperatures warmer than approximately -35°C , ice particles form via heterogeneous nucleation on insoluble IN. Because of its importance, heterogeneous nucleation has been studied extensively in the laboratory and field (e.g., Vali 1974; Deshler 1982; Cooper 1986; Rogers 1982; Meyers et al. 1992; Pruppacher and Klett 1997, hereafter PK97). Four distinct modes of heterogeneous nucleation have been identified: deposition nucleation, condensation freezing, contact freezing, and immersion freezing. Empirical dependencies of IN concentration as a function of temperature or ice supersaturation have been suggested (e.g., Fletcher 1962; Cooper 1986; Meyers et al. 1992). Classical theory includes equations for the critical energy and radius of an ice germ to determine the nucleation rate per unit area of insoluble substrate. Khvorostyanov and Curry (2000, 2005) extended this theory to derive expressions for heterogeneous nucleation as a function of temperature and supersaturation with account for misfit strain. A major premise of this theory, similar to DeMott et al. (1997, 1999), is that internally mixed aerosols (i.e., particles containing both soluble and insoluble components) that serve as CCN may also serve as IN, but, as opposed to droplet activation, the insoluble fraction determines the nucleating ability of the particle. This formulation establishes a link between the temperature and humidity dependence of the IN concentration and the aerosol chemical and physical characteristics. At temperature colder than $\sim -35^\circ\text{C}$, homogeneous freezing of haze particles may be the dominant nucleation mechanism (e.g., Sassen and Dodd 1989; Jensen et al. 1998).

Ice nucleation is formulated in the model in terms of three mechanisms: condensation freezing on partially soluble aerosols, homogeneous freezing on soluble or partially soluble aerosols, and contact freezing of drops due to collection of insoluble aerosols (homogeneous freezing of drops is assumed to occur instantaneously at temperatures less than -40°C). Here we assume that aerosols are internally mixed (containing both soluble and insoluble material) based upon chemical analysis of arctic haze (Borys 1989), except for a small subset of insoluble particles that may initiate contact freezing.

Condensation freezing is assumed to occur on deliquesced, internally mixed aerosols consisting of an in-

soluble nucleus surrounded by a film of soluble material. The probability of a particle freezing is given by

$$P_{CF} = 1 - \exp[-J_{CF}(r_N)\Delta\tau], \quad (9)$$

where $\Delta\tau$ is time period over which the freezing occurs and r_N is the radius of the insoluble nucleus determined from the soluble fraction and size of the aerosol particle. The term J_{CF} is the rate of germ formation through condensation freezing as a function of the activation energy at the solution–ice interface, ΔF_{act} , and critical energy of ice germ formation, ΔF_{cr} (Pruppacher and Klett 1997). Khvorostyanov and Curry (2000, 2005) derive expressions for ΔF_{act} and ΔF_{cr} as a function of r_N , T , and S .

The probability of homogeneous freezing of a wet aerosol particle is expressed as

$$P_{HF} = 1 - \exp\left[-J_{HF}(r_w)\frac{4\pi}{3}(r_w^3 - r_N^3)\Delta t\right], \quad (10)$$

where the rate of germ formation per volume of solution, J_{HF} , is calculated following Khvorostyanov and Sassen (1998), and r_w (r_d) is the radius of the deliquesced aerosol with account for curvature and solute effects following Khvorostyanov and Curry (1999a).

The potential number of crystals nucleated through homogeneous freezing and condensation freezing on aerosols is calculated by integrating over the aerosol size distribution given by (3). As described by Khvorostyanov and Curry (2005) and Khvorostyanov et al. (2005), there is a negative feedback between the ice crystal concentration and ice supersaturation since crystal growth quickly reduces ice supersaturation below the threshold value for nucleation, limiting the number of crystals nucleated to a small fraction of the total aerosol. Modeling results suggest that this process may occur over time scales of a few seconds or less (Khvorostyanov et al. 2005). Thus, ice nucleation will not be resolved in most modeling applications. To address this problem, parcel simulations are performed using a 1-s time step to determine the crystal concentration for several initial values of temperature, RH, and cooling rate or effective vertical velocity, and the results are incorporated into a lookup table, representing an improvement over the M05a scheme. The major drawback to this approach is that a new lookup table must be created if the aerosol size or solubility is modified; the dimensionality of the table would be far too large otherwise. Subgrid vertical velocity due to turbulence is neglected since higher-frequency perturbations have little impact on ice nucleation (Jensen and Pfister 2004), although gravity wave perturbations may be important (Jensen et al. 2005). Another issue is that the crystal growth rate and thus crystal concentration are a

function of the atmospheric pressure. However, for the effective vertical velocities less than $\sim 5 \text{ cm s}^{-1}$ simulated here, the predicted crystal concentration only varies by 10%–15% between 250 and 1000 mb.

Contact freezing of cloud droplets and rain provide another mechanism for the formation of ice in the model. The number of contact nuclei, N_{IN} , is a function of temperature following Meyers et al. (1992). However, to initiate freezing, the contact nuclei must be collected by drops through the combined effects of Brownian motion and phoretic forces (i.e., diffusio-phoresis and thermophoresis; e.g., Young 1974; PK97). Since phoretic forces depend upon the vapor density and temperature differences between the drop and its environment (see Young 1974), collection rates will vary between local updrafts and downdrafts that are not resolved by the model. Since thermophoresis is dominant, the net effect is to inhibit contact nucleation in subgrid regions of supersaturation and enhance contact nucleation in subgrid regions of subsaturation (Young 1974; Cotton et al. 1986). Here, we assume that the net effects are phoretic forces are approximately balanced over the grid cell as a whole, so that the grid-averaged collection rates are dominated by convective Brownian diffusion, which is not impacted by subgrid regions of subsaturation or supersaturation. The collection rate through convective Brownian diffusion, dN_{IN}/dt , is given by (Slinn and Hales 1971),

$$\frac{dN_{IN}}{dt} = 2\pi D_B D_w N_{IN} (1 + 0.3\text{Re}^{(1/2)}\text{Sc}^{(1/3)}), \quad (11)$$

where D_w is the drop diameter, Re is the Reynolds number of the falling drop, Sc is the Schmidt number, and the diffusivity D_B is given by

$$D_B = kT \frac{(1 + \text{Kn})}{3\pi D_{IN}\mu}. \quad (12)$$

Here, k is Boltzman's constant, μ is the dynamic viscosity, Kn is the Knudsen number, and D_{IN} is the diameter of the contact nuclei. The size distribution of contact nuclei is assumed to be monodisperse with a diameter of $0.5 \mu\text{m}$. The sensitivity of the model to changes in the size and number concentration of contact nuclei is tested in section 7. Each collected nuclei is assumed to result in the freezing of one drop.

The number of contact nuclei collected in a time step is a tiny fraction of N_{IN} . However, as suggested by Z05, depletion of contact nuclei may be important when accumulated over time, so that the number of contact nuclei is primarily controlled by the entrainment of particles into the cloud layer from above, since IN sources at the ice-covered surface were limited outside of leads

(Curry et al. 2000; Rogers et al. 2001). We leave an investigation of possible contact nuclei depletion and entrainment for future work and currently assume a steady supply of contact nuclei so that N_{IN} is constant for a given temperature.

4. Model configuration and forcing

The MM5 is a nonhydrostatic model that includes a number of parameterizations for treating: 1) shortwave and longwave radiative transfer, 2) boundary layer (BL) and turbulence processes, 3) surface processes and exchange with the overlying atmosphere, 4) cumulus convection, and 5) cloud microphysics. The nonhydrostatic momentum equations are solved using the time splitting method for sound wave stability described in Grell et al. (1994). The shortwave and longwave radiative transfer follows Breigleb (1992a,b). Turbulent fluxes in the atmosphere and between the surface and atmosphere are parameterized following the 1.5-order prognostic TKE scheme described by Janjic (1994). Heat transfer through the surface is predicted using a multi-layer soil or sea ice and snow model depending upon the surface type (Bromwich et al. 2001). The surface latent and sensible heat fluxes over ocean points are calculated by averaging the separate contributions from open water and sea ice in each grid cell depending upon the specified sea ice concentration. Here, a sea ice concentration of 0.95 is assumed for all ocean points in the model domain consistent with Special Sensor Microwave Imager retrievals (Cavalieri et al. 2004). The microphysics scheme is coupled to the radiative transfer using water contents and effective radii diagnosed from the predicted number concentrations and mixing ratios. Cloud fraction within a grid cell is assumed to be 1 if the water content exceeds $10^{-4} \text{ g kg}^{-1}$, and 0 otherwise. Cloud optical properties are calculated following Slingo (1989) and Ebert and Curry (1992) for droplets and ice, respectively. Turbulent transport is calculated for cloud droplets and ice, but is neglected for precipitation (rain and snow). The parameterization of shallow and deep cumulus convection is neglected since convection is limited over sea ice, with the exception of convective plumes emanating from leads (e.g., Pinto and Curry 1995).

MM5 offers the flexibility of grid nesting. We utilize two domains centered on the SHEBA site (Fig. 1). The outer domain has a grid spacing of 60 km and a time step of 1 min. The inner domain has a grid spacing of 20 km and time step of 20 s. Results from the inner domain are presented here. The baseline simulation is performed with 34 vertical levels and 15 levels in the lowest

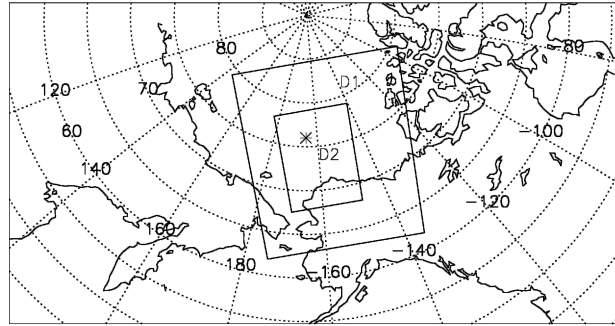


FIG. 1. Location of the MM5 domains. The SHEBA site is indicated by *, D1 and D2 indicate the outer and inner model domains, respectively.

1 km (vertical resolution is modified in sensitivity tests). The initial and lateral boundary conditions are specified using the 2.5° National Centers for Environmental Prediction (NCEP) Global Data Assimilation System dataset (Kalnay et al. 1996). The period simulated is from 0000 UTC on 4 May to 1200 UTC on 5 May. The quantitative comparison with observation consists of the period 1200 UTC 4 May to 1200 UTC 5 May to allow for a 12-h spinup of clouds corresponding to the “cold start” (i.e., no initial cloud water in the simulation). The processes of cloud formation and maintenance are analyzed over the entire simulation period. We chose not to perform any horizontal averaging of the model output in comparing with the column SHEBA observations since the predicted cloud deck tends to be horizontally uniform.

Aerosol properties are based on CN and CCN aircraft measurements taken during clear-sky periods in May 1998 as part of FIRE ACE (Yum and Hudson 2001). We chose aerosol properties measured during clear-sky conditions to avoid low concentrations associated with nucleation and particle scavenging in the cloud layer and below. The aerosol number concentration, N_a , is given by observed CN concentrations that ranged from ~ 350 to 700 cm^{-3} , with the larger values occurring at higher altitudes. These aerosol concentrations are similar to those obtained by Radke et al. (1984) during an arctic haze event. Since detailed measurements of aerosol size and composition were lacking, we must infer values for the aerosol parameters needed by the model (i.e., size and composition) from the observed CCN activity spectra and reports in the literature. A soluble volume fraction of 75% (with the soluble portion consisting of ammonium sulfate) is specified based upon the occurrence of high-sulfate aerosols in the Arctic during springtime haze events (Borys 1989). The aerosol size parameters (r_{min} and μ) were found by matching CCN spectra calculated by (4)

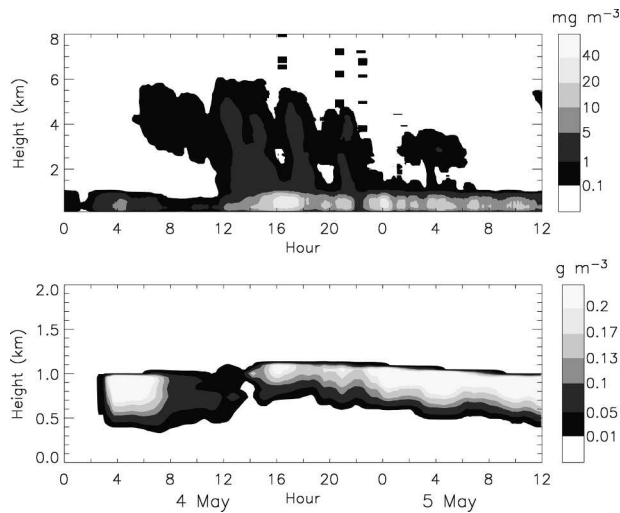


FIG. 2. Ground-based retrievals of (a) ice water content and (b) liquid water content at SHEBA. Data are 42-min moving averages. Retrieved LWC profiles are calculated by assuming adiabatic lifting of parcels from the lidar-derived cloud base, with the LWP constrained by MWR retrievals.

(using the observed number concentration and assumed composition) with observed CCN spectra obtained during the three flights that encountered clear-sky conditions. The sensitivity of the model to modifi-

cation of the aerosol characteristics will be described in a forthcoming companion paper.

5. Case description

A low-level MPS formed over the western Arctic basin in late April and persisted nearly continuously at SHEBA until mid-May under generally weak synoptic-scale dynamics (Curry et al. 2000; Wylie 2001; Z05). Thin upper-level ice clouds appeared at 0600 UTC on 4 May over the SHEBA site, merging with and seeding the lower cloud at 1200 UTC before dissipating at 0600 UTC on 5 May (Fig. 2a). The LWC in the MPS approached zero during this seeding event (Fig. 2b); however, the LWC began to decrease before seeding occurred, implying that additional mechanisms acted to reduce the amount of supercooled water in the cloud. On 4 May, NCEP–NCAR reanalyses indicated an anticyclone to the south and west of the SHEBA site centered near the Chukchi Sea, with a weak cyclone to the east. By 1200 UTC 5 May, the anticyclone strengthened and moved into the Beaufort Sea to the south and east of SHEBA. The BL was well mixed from the surface to cloud top, with a cloud-top temperature of ~ 250 and 2–3-K temperature inversion above the BL (Fig. 3). An inversion in the water vapor mixing ratio was also

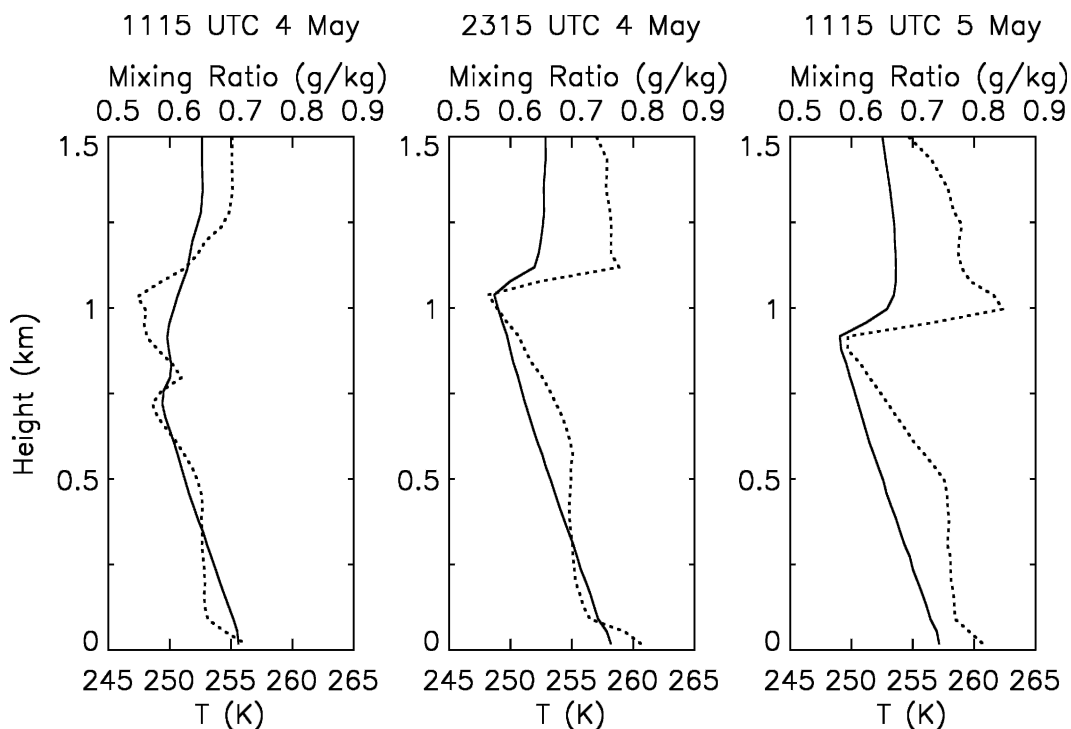


FIG. 3. Observed temperature, T (solid), and water vapor mixing ratio (dotted) obtained from sounding/tower measurements at SHEBA.

present above cloud top. The ice hydrometeor field exhibited significant temporal and spatial variability; the liquid layer exhibited comparatively less variability over similar scales (Lawson et al. 2001; Z05). Significant variability over time scales less than ~ 10 – 15 min (appearing as vertical fallstreaks in the low-level cloud) is also indicated by the time series of MMCR reflectivity (which is dominated by ice) at SHEBA (Fig. 4). The retrieval data presented here are 42-min moving averages, corresponding with an advective time scale over the 20-km model grid cell assuming a wind speed of 8 m s^{-1} . This averaging filters high-resolution variability exhibited by the original data. Similarly, the satellite retrieval data are horizontally smoothed using a 20-km moving box average.

6. Model results

Time–height plots of the modeled IWC and LWC for the grid cell incorporating the SHEBA site shown in Fig. 5 indicate that the model produces a low-level MPS surmounted and seeded by higher ice clouds, similar to retrievals. Both the modeled and observed low-level clouds are liquid topped, with light snow continuously falling to the surface (0.5 mm of liquid-equivalent precipitation accumulates at the surface in the simulation compared with the trace amount reported by surface observations). This canonical structure of mixed-phase clouds has been observed in both polar (e.g., Hobbs and Rangno 1998; Pinto 1998; Rangno and Hobbs 2001; Lawson et al. 2001; Curry et al. 2000; Korolev et al. 2003; Z05) and midlatitude (e.g., Cunningham 1957; Hobbs and Rangno 1985; Rauber and Tokay 1991) regimes.

The predicted top of the MPS is initially about 500 m lower than indicated by the retrieved LWC (see Fig. 2); however, this bias is reduced over time. The cause of this bias is uncertain, but may be due to potential deficiencies in the BL parameterization, vertical velocity, or initialization fields (particularly since the bias is reduced over time). A comparison between the aircraft observed and retrieved cloud top suggest that horizon-

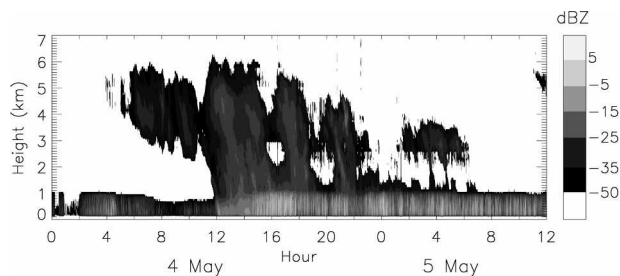


FIG. 4. MMCR reflectivity at SHEBA.

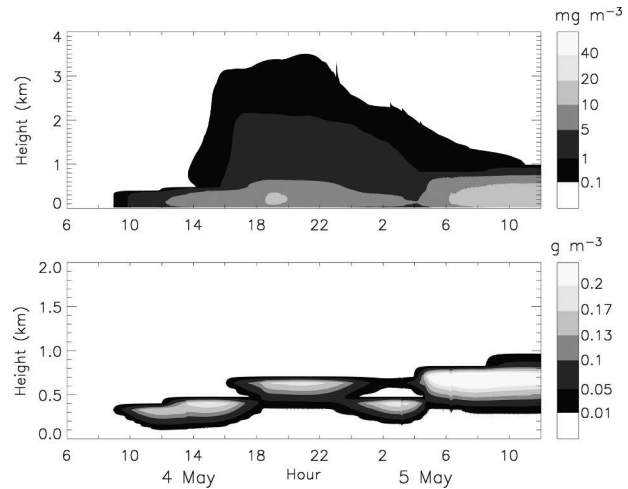


FIG. 5. Modeled (a) ice water content and (b) liquid water content for the SHEBA grid.

tal variability of about 100 m occurred over a few tens of kilometers (Z05). The simulated mid- and upper-level ice cloudiness is also less extensive than observed above about 3 km. However, the predicted IWC between ~ 1 and 2 km is similar to retrievals. Parallel simulations of this case using other bulk microphysics parameterizations also fail to capture the observed upper-level cloudiness above 3 km (Morrison and Pinto 2005, manuscript submitted to *Mon. Wea. Rev.*, hereafter MP05). This suggests that poor simulation of the upper-level cloud results from parameters/formulations common to all of the schemes or factors not directly related to the microphysics (e.g., upper-level humidity bias in the NCEP reanalyses). Although this study focuses on the MPS, the upper cloud may be important since it impacted the MPS through seeding and potential radiative interaction. However, this impact was probably limited since IWCs in this cloud were small $< 5 \text{ mg m}^{-3}$. This is further suggested by the retrieval data, which show that 1) although LWC decreased around 0800 UTC 4 May, this occurred prior to seeding, and 2) LWC content began increasing at 1400 UTC, shortly after the seeding began (see Fig. 2). These changes in LWC may have been more related to changes in the large-scale vertical velocity as suggested by model results described in section 7. A sensitivity test with increased ice nucleation rate in the upper cloud suggests that liquid water is depleted in the BL if the crystal concentration in the upper cloud is increased by a factor of 2 to 3.

Once liquid water appears in the SHEBA grid cell at 0900 UTC 4 May, the model reproduces the overall trend to increasing LWC with time, although the mean and maximum values are somewhat smaller than retrieved (Table 1). Even though the modeled LWP often

TABLE 1. Modeled and retrieved liquid (g m^{-3}) and ice water contents (mg m^{-3}) for the boundary layer stratus at SHEBA. Liquid and ice water contents are screened for values $>0.05 \text{ g m}^{-3}$ and 1 mg m^{-3} , respectively. Statistics are calculated for the period 1200 UTC 4 May to 1200 UTC 5 May.

	LWC			IWC		
	Mean	Std dev	Max	Mean	Std dev	Max
Modeled	0.135	0.064	0.310	7.3	3.4	15.7
Retrieved	0.159	0.072	0.344	8.5	5.7	32.7

differs substantially from the MWR retrievals (exceeding the retrieval uncertainty of 10 g m^{-2}), the overall trend is reasonably captured (Fig. 6). Modeled and retrieved IWCs in the BL cloud are generally between about 5 and 15 mg m^{-3} , with mean values quite similar between the retrievals and simulation (Table 1). However, the retrievals indicate much more variability over time scales of 1–4 h (even after temporal smoothing is applied, see section 5). This difference may reflect ice formation that was controlled by entrainment of contact nuclei from aloft in the real cloud as suggested by Z05, producing enhanced amounts of ice during periodic episodes of subsidence. In the model, a continuous supply of contact nuclei is assumed (see section 3b). In addition, the enhanced production of ice locally in regions of droplet evaporation (due to the impact of thermophoresis on the collection rate of contact nuclei, see section 3b) may have produced the high-resolution variability over time scales less than about 10–15 min in the low-level cloud. This appears as vertical fallstreaks in the image of radar reflectivity (see Fig. 4) that were filtered by the temporal smoothing used in Fig. 2.

The simulated droplet number concentration is relatively constant in height and time for the SHEBA grid cell (Fig. 7a). In most of the MPS, values range from about 200 to 300 cm^{-3} . This implies that about 70% of the aerosols were activated as droplets in the simulation. A similar CN removal rate was inferred from in situ observations taken on 4 May (Yum and Hudson 2001). The predicted crystal concentration of about $0.5\text{--}2 \text{ L}^{-1}$ (mean of 0.9 L^{-1} in the BL cloud; Fig. 7b) is

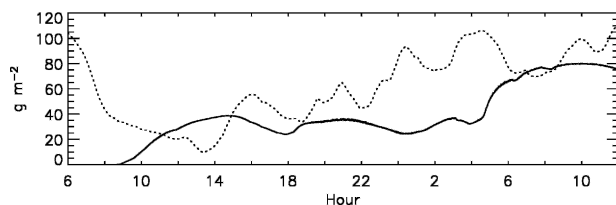


FIG. 6. Modeled (solid) and MWR-derived (dotted) liquid water path at SHEBA. MWR data are 42-min moving averages.

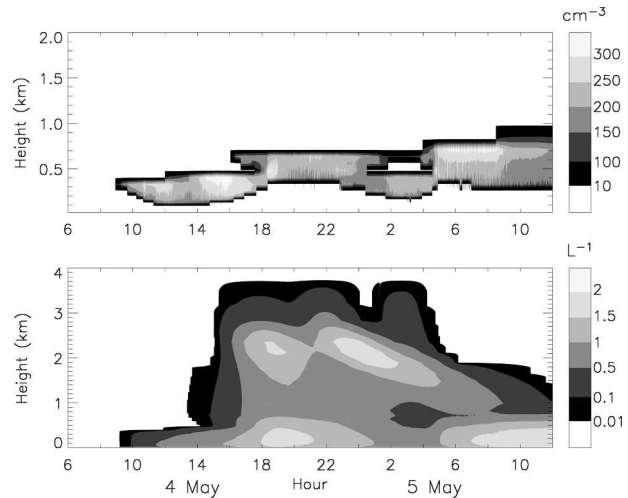


FIG. 7. Modeled (a) droplet number concentration and (b) crystal concentration for the SHEBA grid.

several orders of magnitude smaller than the droplet concentration. Previous observations of arctic stratus (e.g., Jayaweera and Ohtake 1973; Bigg 1996; Pinto 1998; Pinto et al. 2001) report similarly low crystal concentrations ($<1 \text{ L}^{-1}$). Interestingly, the crystal concentration is similar between the upper and lower clouds even though different ice nucleation mechanisms occur in these clouds (see section 7). Values of N_i of a few per liter are similar to in situ aircraft observations using the 260X probe. However, the 260X was found to undercount same-sized particles relative to other instruments (Lawson 2003). The CPI showed ice crystal concentrations exceeding modeled values by 1 to 2 orders of magnitude (Lawson 2001). However, at this point in time it is difficult to assess the accuracy of the CPI-derived ice concentrations (Z05), particularly with regard to the potential for shattering of crystals by the instrument itself during flight.

Vertical profiles of the simulated and in situ observed LWC, droplet concentration, and droplet effective radius are shown in Fig. 8. The modeled profiles (time average ± 1 std dev) are calculated over the 3-h period of 2100 UTC 4 May to 0000 UTC 5 May, with in situ observations obtained during aircraft ascent and descent legs flown at approximately 2154 and 2330 UTC 4 May. The profiles are normalized to cloud top to remove the bias associated with cloud height described previously. Both the modeled and observed LWC profiles are close to adiabatic, corresponding with a well-mixed layer extending from the surface to cloud top. Observations have shown that liquid water in weakly or nonprecipitating arctic stratiform clouds is often adiabatically distributed (Curry 1986; Herman and Curry

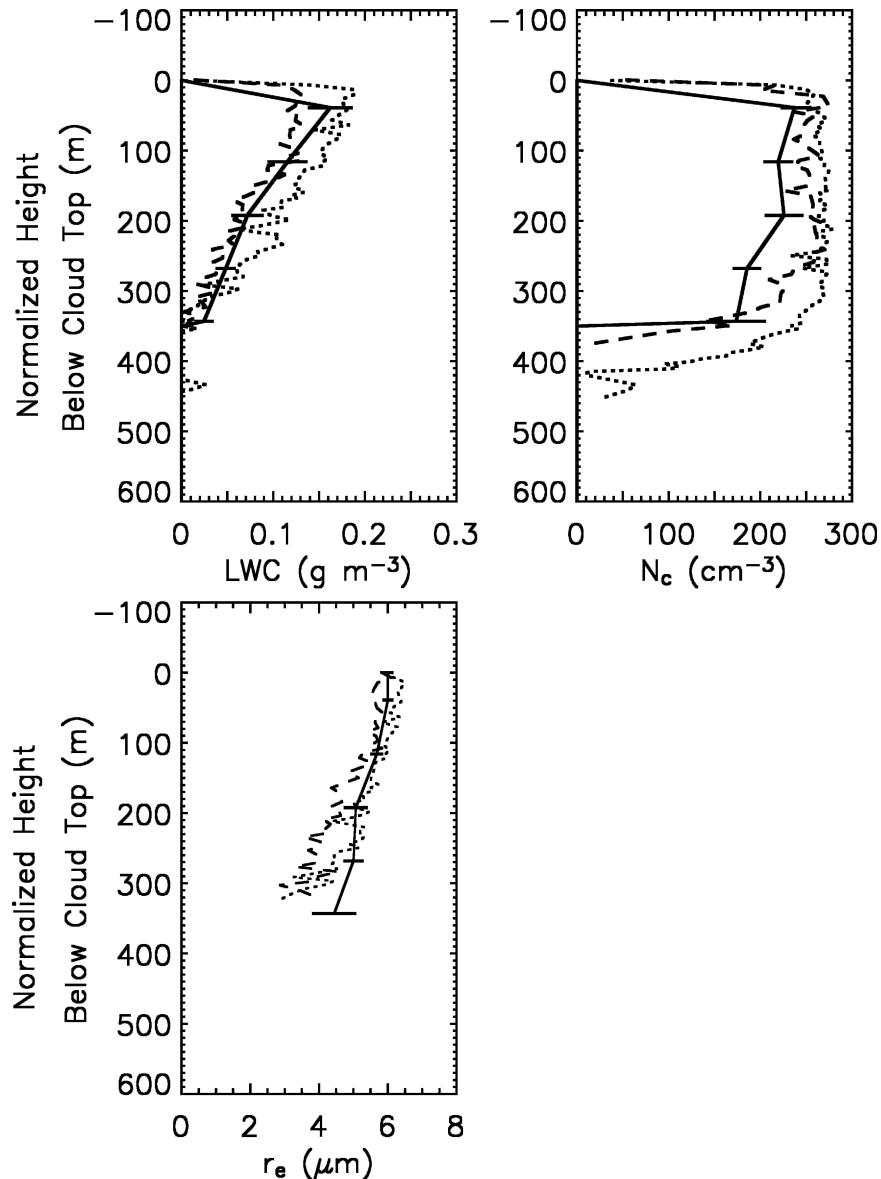


FIG. 8. Modeled (solid) and in situ observed vertical profiles of (a) liquid water content, (b) droplet number concentration, N_c , and (c) droplet effective radius, r_e , at SHEBA FIRE ACE. In situ values were obtained during the 2154 UTC 4 May descent (long dash) and 2320 UTC 4 May ascent (dotted) legs. Modeled values are averages over the period 2100 UTC 4 May to 0000 UTC 5 May, with horizontal bars indicating ± 1 std dev. Data are normalized to height below cloud top.

1984; Hobbs and Rangno 1998; Pinto 1998; Curry et al. 2000; Lawson et al. 2001; Z05). Note that in the simulation, adiabatic profiles are mostly a consequence of the vertical turbulent mixing of cloud water rather than adiabatic growth (evaporation) of droplets in local updrafts (downdrafts). This is reflected by the vertical distribution of latent heating and thus temperature; the simulated BL is vertically constant with respect to potential temperature, rather than equivalent potential

temperature (this occurs because the BL scheme mixes potential rather than equivalent potential temperature within the cloud layer). Note that during corresponding times, the MWR-derived LWPs (which were used to constrain the retrieved LWCs) are within 5% of the aircraft-derived values (Z05). Horizontal transects of the aircraft at constant altitude show LWCs varying by up to 25% of their mean (Z05).

The simulated and observed droplet number concen-

trations are fairly uniform through the depth of the MPS, with modeled values generally between about 190 and 230 cm^{-3} , slightly smaller than observed concentrations of about 200–270 cm^{-3} (Fig. 8b). Note that increasing vertical resolution increases the predicted values of droplet concentration by 20% (see section 7). The uniformity of droplet number concentration with height is common in both arctic (e.g., Curry 1986; Z05) and midlatitude (e.g., Nicholls 1984; Duynkerke et al. 1995) stratiform clouds with weak precipitation development. The predicted and observed droplet effective radii are generally between 3 and 6 μm and exhibit an overall increase with height (Fig. 8c). The relatively small droplet sizes limit coalescence and warm-rain production. The modeled droplet concentration and effective radius exhibit most variability near cloud base, where the mean modeled effective radius is about 0.5–1 μm larger than aircraft measurements.

Modeled and retrieved IWC profiles (time average ± 1 std dev) for the period 1800 UTC 4 May to 0200 UTC 5 May are shown in Fig. 9 (profiles are normalized to the top of the liquid layer). Both the modeled and retrieved profiles exhibit a maximum below the base of the liquid layer with smaller values near the surface. The modeled IWCs during this period tend to be smaller (larger) in the lower (upper) portion of the

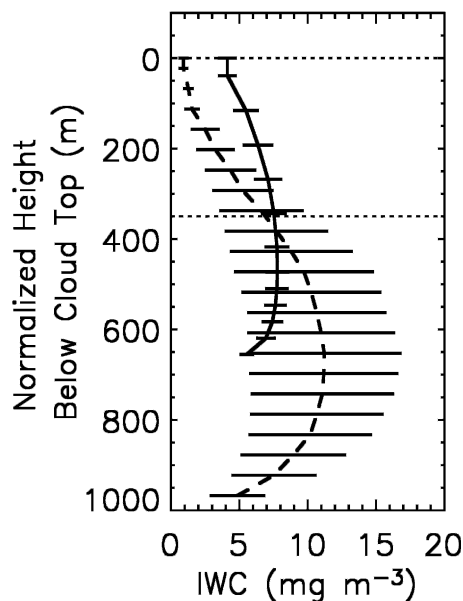


FIG. 9. Modeled (solid) and retrieved (long dash) profiles of ice water content at SHEBA FIRE ACE. Modeled and retrieved values are averages over the period 2100 UTC 4 May to 0000 UTC 5 May, with solid horizontal bars indicating ± 1 std dev. Data are normalized to height below the top of the liquid layer. The approximate aircraft-observed and modeled boundaries of the liquid layer are indicated by the horizontal dotted line.

cloud layer, although most modeled values are within the retrieval uncertainty. Differences between the modeled and retrieved profiles may be partly due to differences in the depth of the cloud layer. We also note that the modeled IWC profile is quite sensitive to the parameterized crystal fall speeds. The retrieval and in situ IWCs for aircraft overpasses of the SHEBA cloud radar, which occurred between 2320 UTC 4 May and 0015 UTC 5 May, are in good agreement (see Z05).

Predicted BL temperatures are warmer than sonde/tower measurements, with the bias increasing by about 1 K every 12 h (Fig. 10a). Near the end of the simulation (1115 UTC 5 May), the BL is about 3 K warmer than observed; differences between the simulated and observed potential temperature are much smaller above the BL. Much of this bias is attributed to errors in the surface energy budget, which lead to overprediction of surface temperature and sensible turbulent heat flux (MP05). Note that a warm bias in the cloud layer may impact the simulated MPS, particularly the partitioning of water between liquid and ice. The underprediction of BL height is consistent with the underprediction of cloud-top height described previously. The depth of the simulated mixed layer increases steadily so that by 1115 UTC 5 May it is similar to observations. The observed evolution of the BL may have been associated with changes in the large-scale vertical velocity (Z05).

The modeled BL tends to be too moist relative to observations (Fig. 10b). The main factor contributing to this bias is the difference in the simulated and observed BL height. Normalized to the top of the BL, the simulated RH profiles are close to observations (not shown). Another factor contributing to differences between the modeled and observed RH profiles is a dry bias in the Väisälä sounding profiles (e.g., Miloshevich et al. 2001; Turner et al. 2003; Wang et al. 2002). For example, the sondes launched at 1115 and 2315 UTC on 4 May indicated a maximum RH of only about 95% even though liquid water was present at these times. The modeled and observed values of relative humidity with respect to ice (RHI) reach about 120% within the BL. These large RHIs lead to rapid depositional growth of ice particles in the simulation. The observed BL also has a fairly deep layer of ice subsaturation extending from the surface that led to sublimation of falling ice.

Satellite retrievals (CAPSR) of cloud optical depth indicate the large horizontal extent of the cloud deck (Fig. 11a; an average of the 1500 UTC 4 May and 0100 5 May overpasses is plotted). The time-averaged (1200 UTC 4 May to 1200 UTC 5 May) modeled cloud optical depth is somewhat smaller, particularly over the east-

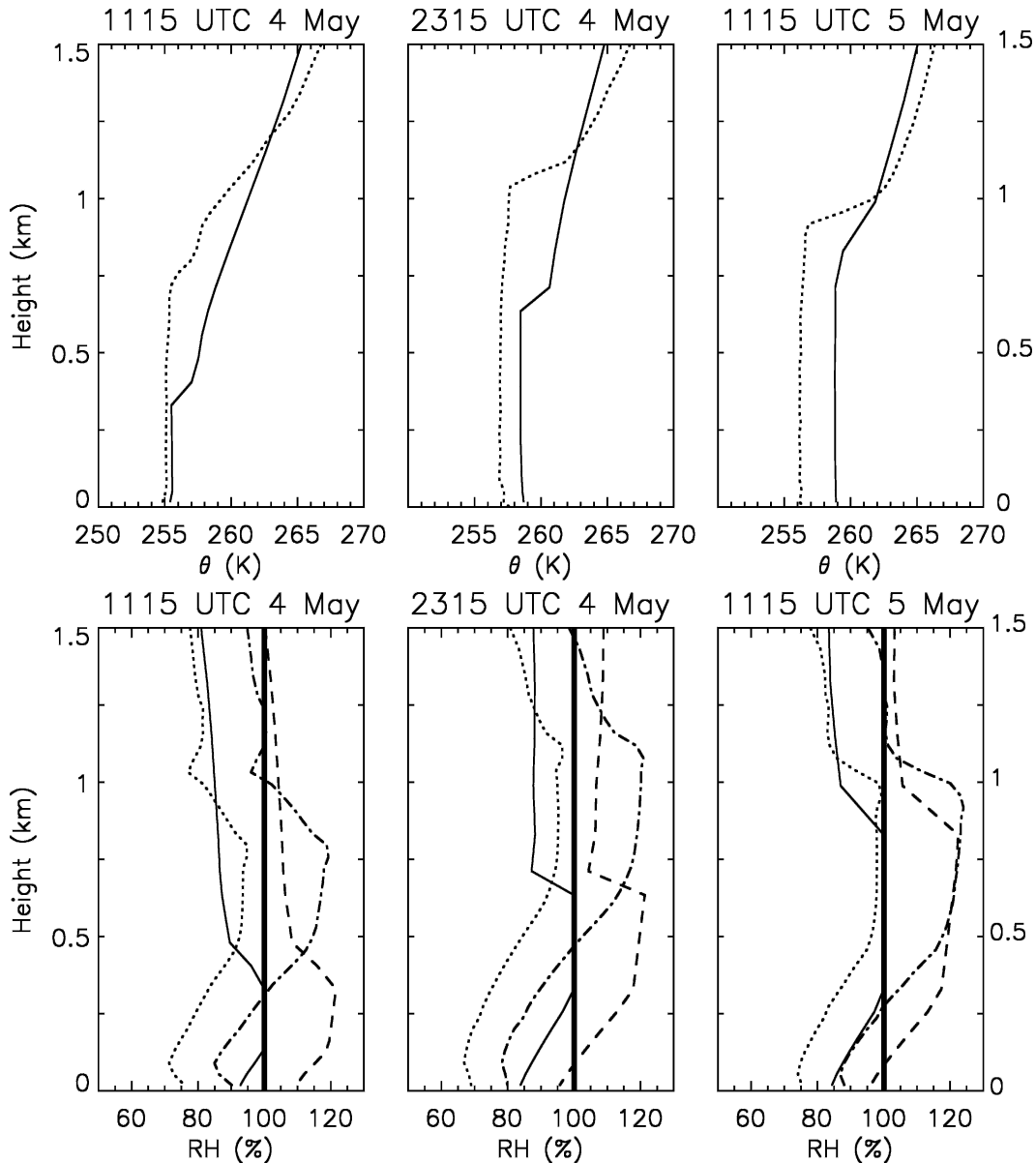


FIG. 10. Modeled (thin solid) and observed (dotted) (a) potential temperature, θ , and (b) RH at SHEBA. Modeled (long dash) and observed (dot-dash) relative humidity with respect to ice is also shown. Observed profiles were obtained from sounding/tower measurements; 100% RH is indicated by the thick solid line.

ern portion of the domain (Fig. 11b). However, the domain-averaged modeled cloud optical depth of 4.3 is fairly close to the retrieved value of 6.2. Uncertainty in the retrieved cloud optical depth is estimated to be 50% (Key et al. 1997); uncertainty is particularly large for overpasses when the sun angle was low (Key 2001). The simulated cloud field appears to exhibit less spatial variability than indicated by retrievals (even after 20-km horizontal smoothing). Heterogeneity in the sea ice surface may contribute to variability in the overlying cloud field, since the surface fluxes are coupled to the cloud

layer during this case (MP05). Retrieval noise may also contribute to spatial variability in the retrieved optical depth field. It should also be noted that both the modeled and satellite cloud optical depths vary significantly with time for a given location, although the cloud deck as a whole remained coherent during the period. The simulated cloud is dominated by supercooled liquid water, with the domain-averaged LWP about 3 times larger than the domain-averaged IWP (Table 2). The time-averaged fraction of grid cells containing supercooled liquid water (defined by a LWP threshold

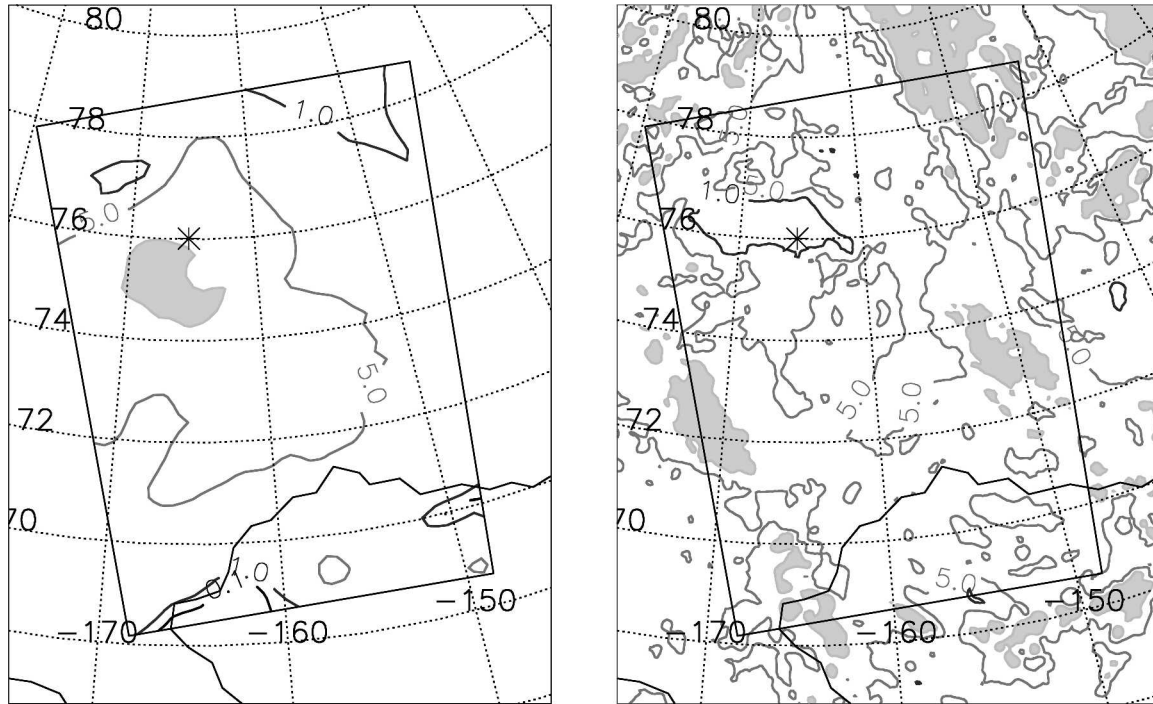


FIG. 11. (a) Modeled and (b) satellite-retrieved (CASPR) cloud optical depth. Modeled values are averages over the period 1200 UTC 4 May–1200 UTC 5 May. Retrieved values are averages of overpasses occurring at ~ 1500 UTC 4 May and 0100 UTC 5 May. The inner model domain is indicated by the box. The SHEBA site is indicated by *. Satellite data were horizontally smoothed using a 20-km moving box average. Regions of cloud optical depth >10 are shaded.

$\geq 1 \text{ g m}^{-2}$) of 67.1% indicates the prevalence of mixed-phase clouds in the simulation. Satellite retrievals indicate that the average liquid water fraction was 65.6% for the two overpasses that occurred during the case.

7. Sensitivity studies of MPS formation and evolution

The formation and maintenance of MPS depends critically on several microphysical and thermodynamic processes (e.g., Rauber and Tokay 1991; Pinto 1998; Harrington et al. 1999; Jiang et al. 2000; Pinto et al. 2001; Rangno and Hobbs 2001; Khvorostyanov et al.

2003). The initial appearance of MPS in the SHEBA grid cell is associated with horizontal advection of cloud water and weak upward motion ($\sim 0.5\text{--}1 \text{ cm s}^{-1}$). The important role of surface turbulent fluxes in maintaining the continuously precipitating cloud layer is described by the budget and sensitivity studies of MP05. While the large-scale vertical velocity impacts the evolution of the MPS (e.g., thinning between 0000 and 0400 UTC 5 May during a period of downward motion), the cloud layer persists even during periods of large-scale downward motion (Fig. 12a). The MPS is largely self-maintained due to strong ($>40 \text{ K day}^{-1}$) cloud-top radiative cooling (Fig. 12b) that promotes condensation and production of TKE via the generation of negative buoyancy. Radiative heating ($>5 \text{ K day}^{-1}$) occurs in the interior of the cloud due to absorption of solar radiation, further destabilizing the layer.

Three primary cloud regions are identified from a time–height plot of the droplet evaporation/condensation rate (Fig. 13). The main region of droplet condensation occurs in the upper portion of the liquid layer corresponding with the strong cloud-top radiative cooling. The interior of the cloud tends to exhibit weak evaporation. Stronger evaporation occurs near cloud base and in the subcloud region due to sedimentation

TABLE 2. Mean (time and domain averaged) LWP, IWP (g m^{-2}), cloud optical depth, τ (unitless), and fraction of grid cells with $\text{LWP} > 1 \text{ g m}^{-2}$, F_l (%), for the baseline, IND, and INI simulations. Values are calculated for the time period 1200 UTC 4 May to 1200 UTC 5 May.

	τ	LWP	IWP	F_l
Base	4.3	19.1	6.0	67.1
IND	8.4	40.6	4.6	70.1
INI	0.6	2.1	4.4	40.5
$D_{\text{IN}} = 0.1 \mu\text{m}$	0.6	2.4	4.5	42.6
$D_{\text{IN}} = 2 \mu\text{m}$	7.5	35.6	5.2	69.9

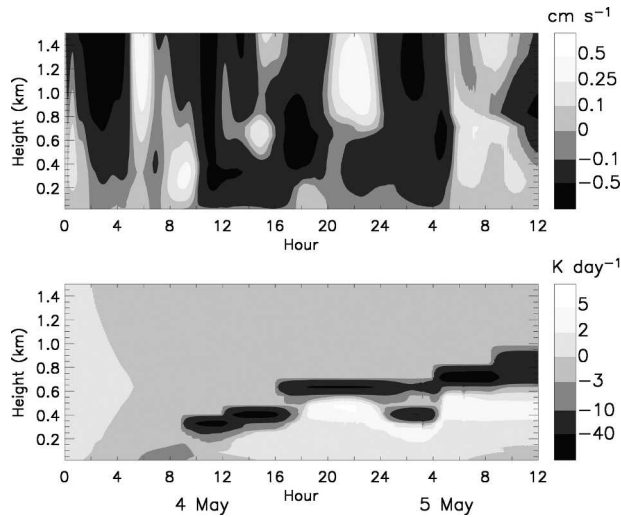


FIG. 12. Simulated (a) grid-scale vertical velocity and (b) radiative heating rate for the SHEBA grid.

and turbulent mixing of liquid water from the main cloud layer into the subsaturated air below. These results are in general agreement with observations of arctic stratus reported by Curry (1986). The condensate produced by radiative cooling in the upper portion of the simulated cloud is mixed downward through turbulent diffusion. A parallel simulation neglecting the turbulent mixing of cloud water [as is standard in MM5 using the Janjic (1994) turbulence parameterization] results in superadiabatic LWC profiles and cloud layers that are far too narrow in the vertical.

Droplet activation in the simulated MPS is concentrated near cloud base and driven by subgrid updrafts (Fig. 14a). The largest rates occur near cloud base mostly because subgrid vertical velocities are greatest in this region. A sensitivity test in which subgrid vertical motion is neglected produces weak droplet activation that is limited to the upper portion of the cloud layer where it is mostly driven by radiative cooling (Fig. 14b). This results in very low droplet number concentrations, with maximum values of only 90 cm^{-3} (Fig. 15a). To

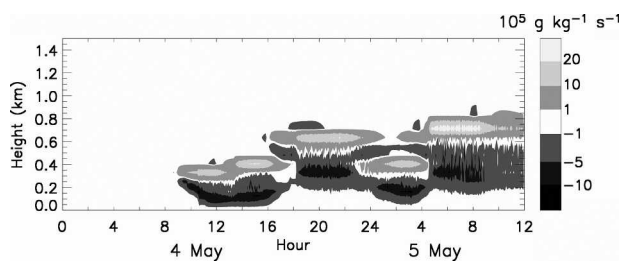


FIG. 13. Simulated liquid water condensation/evaporation rate for the SHEBA grid. Data are 5-min averages.

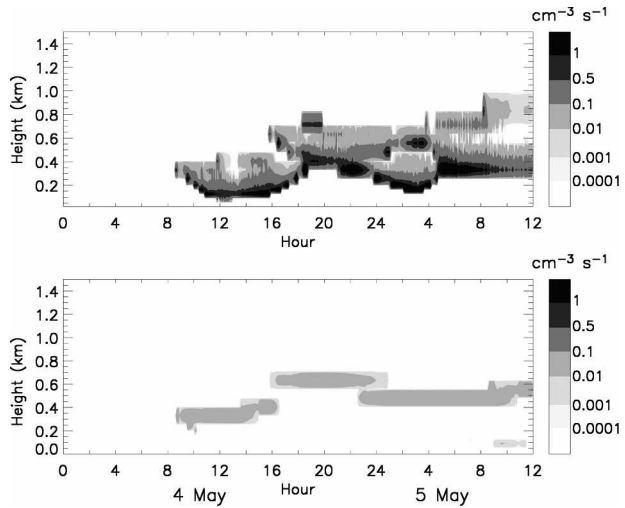


FIG. 14. Droplet activation rate for (a) the baseline simulation and (b) the simulation with no subgrid vertical velocity, for the SHEBA grid. Data are 5-min averages.

test how microphysical processes and turbulence impact the droplet number concentration, a sensitivity test is also performed in which the droplet number concentration is diagnosed from the CCN concentration using (7) rather than prognosticated. This simulation produces somewhat larger droplet concentrations near cloud base and much lower concentrations near cloud top (Fig. 15b). It also produces much lower cloud boundaries and less liquid water overall compared with the baseline simulation. These results illustrate in particular the importance of turbulent transport as a source for droplet number in the middle and upper part

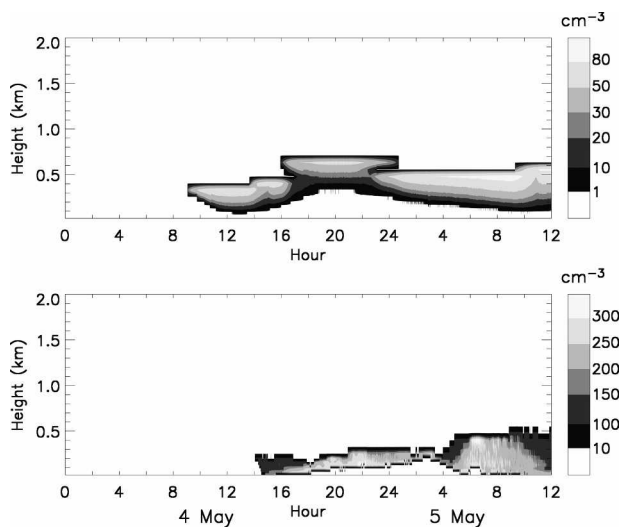


FIG. 15. Droplet number concentration for (a) the simulation with no subgrid vertical velocity and (b) simulation with diagnostic droplet concentration, for the SHEBA grid.

of the cloud. Both turbulence and microphysical processes (mostly evaporation) act to reduce number concentration near cloud base.

The initial formation of ice in the simulated MPS occurs mostly as a result of the contact freezing of droplets. Temperatures are generally too warm to promote ice nucleation via condensation freezing since this mode is limited to temperatures colder than about 251 K at water saturation given the aerosol size and composition described in section 4 (Fig. 16). Note that in the upper cloud (in the SHEBA grid cell), which is below 251 K, condensation freezing on aerosol is the ice nucleating mechanism. This is consistent with studies (e.g., Young 1974; Hobbs and Rangno 1985) suggesting that particles are active at significantly warmer temperatures in the contact mode compared to other nucleation modes. We note that the threshold temperature for condensation freezing is sensitive to the aerosol size and solubility (MAP05). The lack of IN (active through condensation freezing) in the simulation is consistent with measurements using CFDC (which did not count contact nuclei) that showed overall low IN concentrations during FIRE ACE; 50% of the 10-s-averaged values were zero (Rogers et al. 2001). The MPS deck is outside the temperature range supporting ice multiplication through the Hallet and Mossop (1974) rime-splintering mechanism. Contact freezing depletes liquid water directly, but also forms ice particles that subsequently uptake water vapor and deplete liquid water through the Bergeron–Findeisen mechanism. The contact freezing of droplets is parameterized in terms of the number concentration and size of contact nuclei (see section 3). The number of contact nuclei is speci-

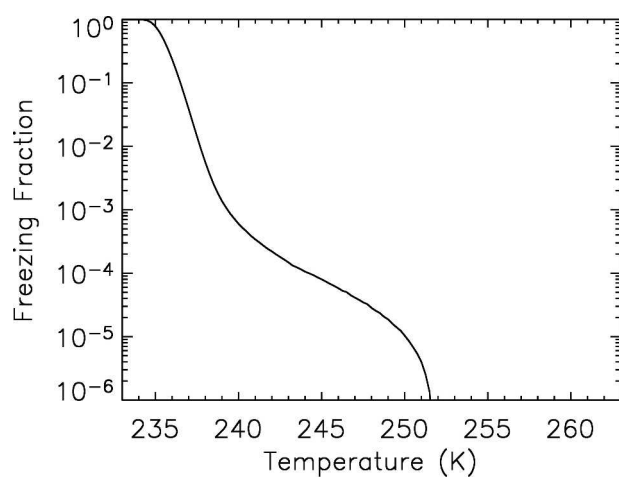


FIG. 16. Condensation freezing fraction of the deliquescent aerosol population ($>0.05 \mu\text{m}$) within 1 min at water saturation as a function of temperature using the aerosol properties described in section 4.

fied as a function of temperature following Meyers et al. (1992) based on a composite of midlatitude observations. This formulation must be regarded as highly uncertain, since observed IN concentrations at a given time and location vary by several orders of magnitude (e.g., PK97). As described in section 3b, the number of contact nuclei in the real cloud system may have been primarily controlled by the balance between depletion and entrainment into the cloud layer from above. The rate of ice nucleation through contact freezing in the simulation (Fig. 17) is similar to the plot of droplet number concentration (see Fig. 7a). However, since the contact freezing rate is also a function of the droplet size, there are regions of low droplet concentration with fairly large nucleation rates, such as occurs in the sub-cloud region near the base of the liquid layer, where large isolated droplets fall into subsaturated air.

Two sensitivity tests are performed to examine how the MPS responds to changes in the number of contact nuclei, one with the baseline value multiplied by a factor of 10 (INI simulation), and the other with the baseline value divided by a factor of 10 (IND simulation). Plots of the time-averaged LWP and IWP over the model domain reveal significant differences between these simulations and baseline (Figs. 18 and 19). Not surprisingly, reducing (increasing) the number of contact nuclei increases (decreases) the mean LWP relative to baseline (Table 2). However, differences in the fraction of grid cells containing liquid water are much smaller. Thus, changes in the number of contact nuclei tend to impact the partitioning of liquid and ice within the MPS, rather than modifying the cloud phase itself. The clouds generally remain mixed phase even with substantial increase in the number of contact nuclei because droplet freezing is self-regulated through a negative feedback (an increase in the droplet freezing rate reduces the amount of cloud water available for subsequent freezing). The modeled cloud optical depth closely tracks the LWP.

LWCs are fairly small, so a modest increase in the concentration of contact nuclei results in a large reduc-

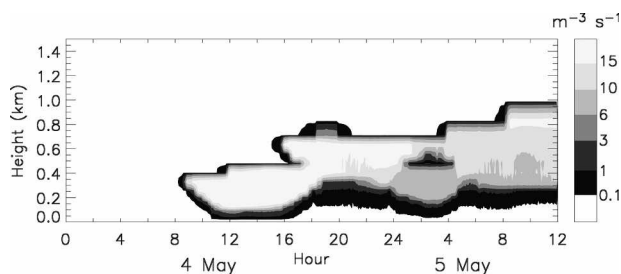


FIG. 17. Rate of ice particle formation through contact freezing of drops for the SHEBA grid.

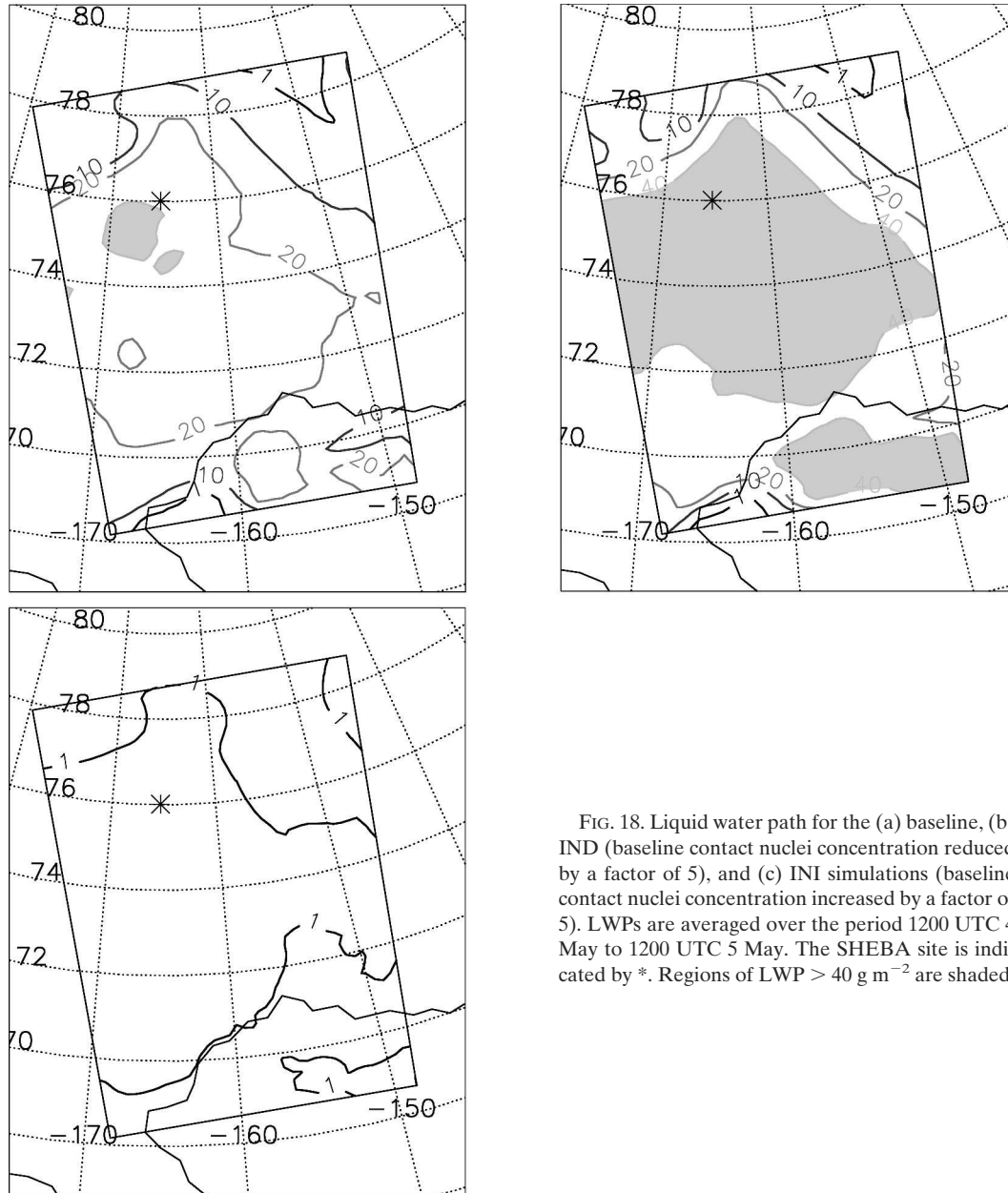


FIG. 18. Liquid water path for the (a) baseline, (b) IND (baseline contact nuclei concentration reduced by a factor of 5), and (c) INI simulations (baseline contact nuclei concentration increased by a factor of 5). LWPs are averaged over the period 1200 UTC 4 May to 1200 UTC 5 May. The SHEBA site is indicated by *. Regions of LWP $> 40 \text{ g m}^{-2}$ are shaded.

tion in the amount of liquid water available for the production of ice and frozen precipitation. Lohmann (2002b) found that increasing the number of contact nuclei led to more rapid glaciation, increased amounts of ice, and increased precipitation in a general circulation model study. Our contrasting results may be due to the unique characteristics of arctic MPS, which contain relatively little condensate and often occur under weak synoptic forcing. Overseeding may have been limited in the real cloud layer because the formation of ice may have depleted the local supply of IN.

Changes in the assumed size of the contact nuclei

also impact the collection rate of the nuclei by droplets (see section 2b) and hence the droplet freezing rate. Sensitivity tests varying contact nuclei diameter D_{IN} are performed. Increasing D_{IN} to $2 \mu\text{m}$ from the baseline value of $0.5 \mu\text{m}$ has an effect quite similar to decreasing the number of contact nuclei by an order of magnitude, with increased cloud optical depth and LWP and decreased IWP (see Table 2). Conversely, decreasing D_{IN} to $0.1 \mu\text{m}$ produces similar results to the run with contact nuclei concentration increased by an order of magnitude, including the decrease in IWP (i.e., overseeding). Note that the population of insoluble particles po-

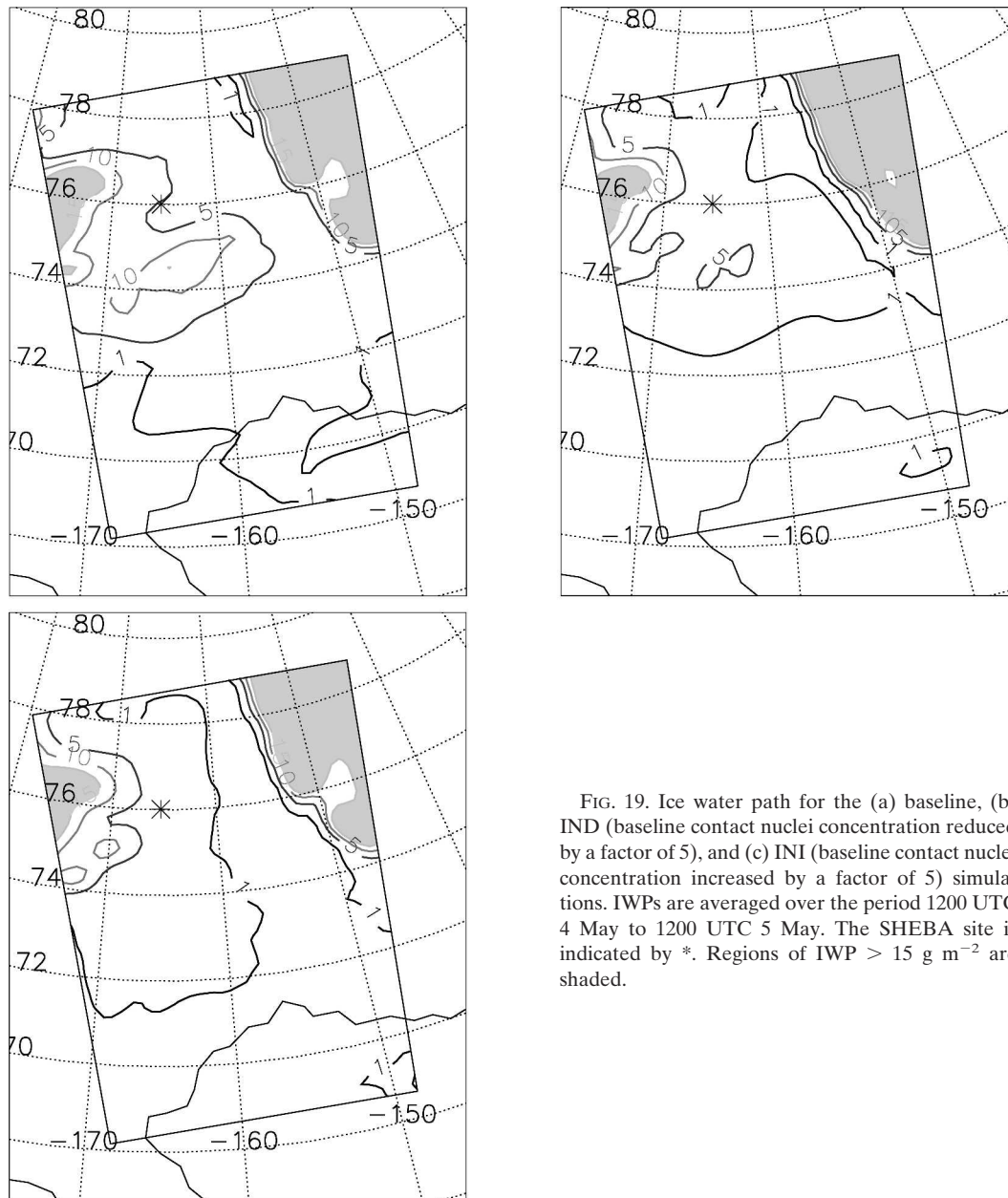


FIG. 19. Ice water path for the (a) baseline, (b) IND (baseline contact nuclei concentration reduced by a factor of 5), and (c) INI (baseline contact nuclei concentration increased by a factor of 5) simulations. IWPs are averaged over the period 1200 UTC 4 May to 1200 UTC 5 May. The SHEBA site is indicated by *. Regions of IWP $> 15 \text{ g m}^{-2}$ are shaded.

tentially serving as contact nuclei has a polydisperse size distribution in the real atmosphere. However, small particles ($< \sim 0.1 \mu\text{m}$) tend to be less active as nuclei (due to smaller frequency of active sites) even though they are associated with larger collection rates (Young 1974). Therefore, these particles may not contribute substantially to the total number of contact nuclei. The size that is preferentially active depends upon temperature as suggested by extensions of classical nucleation theory, with smaller particles only active at colder temperatures (Khvorostyanov and Curry 2005). Therefore, we hypothesize that the observed increase in number

concentration of active nuclei at colder temperatures (e.g., Meyers et al. 1992) is due to the activation of smaller particles (in addition to the larger particles) within the distribution.

Increasing the vertical resolution in the lowest 1.5 km by a factor of 2 illustrates interactions between the radiative transfer, turbulent mixing, and cloud microphysics. For example, with increased vertical resolution, the cloud-top radiative cooling is better resolved, resulting in larger cooling rates concentrated near cloud top. This further destabilizes the BL and produces larger TKE in the cloud layer (average of $0.20 \text{ m}^2 \text{ s}^{-2}$ com-

pared to the baseline value of $0.16 \text{ m}^2 \text{ s}^{-2}$ for the SHEBA grid). With increased turbulence and thus larger subgrid vertical velocities, the droplet number concentration is 20% larger in the sensitivity simulation for the SHEBA grid. Decreasing the vertical resolution in the lowest 1.5 km by a factor of 2 has little impact on the simulation.

8. Summary and conclusions

In this study, a new two-moment bulk microphysics scheme was incorporated into the polar version of the PSU-NCAR MM5 to simulate a MPS deck observed on 4–5 May 1998 during SHEBA FIRE ACE. Model results were compared to detailed in situ observations and remotely based retrievals, and the impacts of nucleation processes, radiative transfer, turbulence, and vertical resolution on the simulated MPS were investigated. The model was able to reproduce several key features indicated by the observations, including

- 1) horizontally extensive, persistent MPS with light snow falling from the cloud base to the surface;
- 2) vertical profile of liquid water that was nearly adiabatic with the cloud layer occurring atop a well-mixed BL coupled to the surface;
- 3) droplet number concentrations of about 200–250 cm^{-3} distributed fairly uniformly through the cloud layer with droplet effective radius increasing with height.

The model was able to reasonably predict the droplet number concentration given aerosol characteristics specified from the observed CN concentrations and CCN activity spectra. Because of the highly variable nature of aerosols in time and space, and the lack of direct measurements of the size-segregated aerosol composition, the impact of varying several aerosol parameters specified in the model will be explored in a forthcoming companion paper. A key aspect of the prediction of droplet activation and droplet number concentration is the need to incorporate subgrid vertical motion. Neglecting subgrid vertical velocity results in weak activation and low droplet number concentrations ($<90 \text{ cm}^{-3}$). These results suggest that detailed treatment of nucleation processes and particle number concentrations is viable in large-scale models provided that the subgrid vertical velocity is adequately parameterized in terms of the grid-scale quantities. Additional work is needed to better characterize the distribution of subgrid vertical velocities in the cloudy BL.

After its initial formation, the simulated MPS was more or less self-maintained by large cloud-top radia-

tive cooling rates that exceeded 40 K day^{-1} . Cloud-top cooling resulted in significant condensation in the upper portion of the cloud. In contrast, the largest droplet activation rates were located near cloud base associated with large subgrid vertical velocities. Evaporation just below cloud base was balanced by sedimentation and turbulent diffusion from the main cloud layer above. These results are in general agreement with previous studies and observations of the cloud-topped BL over the arctic pack ice (e.g., Curry 1986; Pinto 1998; Harrington et al. 1999; Jiang et al. 2000).

The primary ice formation mechanism in the simulated MPS was contact freezing of droplets. Temperatures were too warm to promote ice nucleation via condensation freezing on aerosol for the given aerosol characteristics. Sensitivity tests showed that the LWP across the horizontal domain was quite sensitive to the specified number of contact nuclei, with increasing (decreasing) contact nuclei concentrations resulting in smaller (larger) LWPs. Increasing the concentration of contact nuclei led to a small decrease in the IWP. This effect is similar to overseeding, which limits the water supply and hence the formation of ice and frozen precipitation. Entrainment may increase the overall droplet freezing rate since it may produce cloud regions with both elevated numbers of contact nuclei and increased collection rate due to phoretic forces (e.g., Young 1974). This suggests that there are numerous uncertainties in the current treatment of contact nucleation; additional studies are needed to address these issues. The future development of a parameterization for the size distribution and concentration of contact nuclei as a function of temperature and characteristics of the insoluble aerosol population should be possible through extensions of classical nucleation theory (Khvorostyanov and Curry 2005). Additional field and laboratory measurements are also needed to better characterize the ice-nucleating properties of various substances found in aerosols.

Several other ice parameters in the model are uncertain and may impact the evolution of the MPS. These include the particle fall speeds, collection efficiency for riming, and crystal habit, to name a few. Previous studies have indicated the importance of these parameters in modeling arctic clouds. For example, increasing the ice particle fall speed led to an increase in the longevity of mixed-phase clouds (Harrington et al. 1999). Lohmann et al. (2003) found that riming and snowfall rates were crucially dependent upon the crystal habit. A more detailed assessment of the sensitivity of the model to the various ice parameters was beyond the scope of this paper but should be addressed in future studies.

Acknowledgments. This research was supported by Grants NSF OPP-0084225 and DOE ARM DE-FG-03-94ER61771. Microwave radiometer data were obtained from the DOE ARM program. Precipitation and rawinsonde measurements were obtained from the SHEBA Project Office at the University of Washington Applied Physics Laboratory. Surface data were obtained from the SHEBA Atmospheric Surface Flux Group. LWC and in situ IWC data were provided by P. Zuidema (CIRES/NOAA-ETL), and ice retrievals were provided by M. Shupe (CIRES/NOAA-ETL). CASPR AVHRR satellite retrievals were provided by J. Key (NOAA NESDIS). The CN and CCN data were made available by J. Hudson (DRI). Ice nuclei data were provided by D. Rogers (CSU). MWR retrievals of LWP were provided by Y. Han (NOAA NESDIS).

REFERENCES

- Albrecht, B. A., 1989: Aerosols, cloud microphysics and fractional cloudiness. *Science*, **237**, 1020–1022.
- Bigg, E. K., 1996: Ice forming nuclei in the high Arctic. *Tellus*, **48B**, 223–233.
- Borys, R. D., 1989: Studies of ice nucleation by arctic aerosol on AGASP-II. *J. Atmos. Chem.*, **9**, 169–185.
- Briegleb, B., 1992a: Delta-Eddington approximation for solar radiation in the NCAR Community Climate Model. *J. Geophys. Res.*, **97**, 7603–7612.
- , 1992b: Longwave band model for thermal radiation in climate studies. *J. Geophys. Res.*, **97**, 11 475–11 485.
- Bromwich, D. H., J. J. Cassano, T. Klein, T. G. Heinemann, K. M. Hines, K. Steffen, and J. E. Box, 2001: Mesoscale modeling of katabatic winds over Greenland with the Polar MM5. *Mon. Wea. Rev.*, **129**, 2290–2309.
- Cavaleri, D., P. Gloerson, and J. Zwally, 2004: *DMSP SSM/I Daily Polar Gridded Sea Ice Concentrations*. National Snow and Ice Data Center, Boulder, CO, CD-ROM.
- Coakley, J. A., and C. D. Walsh, 2002: Limits to the aerosol indirect radiative effect derived from observations of ship tracks. *J. Atmos. Sci.*, **59**, 668–680.
- Cooper, W. A., 1986: Ice initiation in natural clouds. *Precipitation Enhancement—A Scientific Challenge*. Meteor. Monogr., No. 43, Amer. Meteor. Soc., 29–32.
- Cotton, W. R., G. J. Tripoli, R. M. Rauber, and E. A. Mulville, 1986: Numerical simulation of the effects of varying ice crystal nucleation rates and aggregation processes on orographic snowfall. *J. Climate Appl. Meteor.*, **25**, 1658–1680.
- Cunningham, R. M., 1957: A discussion of generating cell observations with respect to the existence of freezing or sublimation nuclei. *Artificial Stimulation of Rain*, H. Weikmann, Ed., Pergamon Press, 267–270.
- Curry, J. A., 1986: Interactions among turbulence, radiation, and microphysics in arctic stratus clouds. *J. Atmos. Sci.*, **43**, 90–106.
- , 1995: Interactions among aerosols, clouds, and climate of the Arctic Ocean. *Sci. Total Environ.*, **160**, 777–791.
- , J. L. Schramm, and E. E. Ebert, 1993: Impact of clouds on the surface radiation balance of the Arctic Ocean. *Meteor. Atmos. Phys.*, **51**, 197–217.
- , W. B. Rossow, and J. L. Schramm, 1996: Overview of arctic cloud and radiation properties. *J. Climate*, **9**, 1731–1764.
- , and Coauthors, 2000: FIRE Arctic Clouds Experiment. *Bull. Amer. Meteor. Soc.*, **81**, 5–29.
- DeMott, P. J., D. C. Rogers, and S. M. Kreidenweis, 1997: The susceptibility of ice formation in upper-tropospheric clouds to insoluble aerosol components. *J. Geophys. Res.*, **102**, 19 575–19 584.
- , Y. Chen, S. M. Kreidenweis, D. C. Rogers, and D. E. Sherman, 1999: Ice formation by black carbon particles. *Geophys. Res. Lett.*, **26**, 2429–2432.
- Deshler, T., 1982: Contact ice nucleation by submicron atmospheric aerosols. Ph.D. dissertation, University of Wyoming, 107 pp.
- Dudhia, J., 1989: Numerical study of convection observed during the Winter Monsoon Experiment using a mesoscale two-dimensional model. *J. Atmos. Sci.*, **46**, 3077–3107.
- Duynkerke, P. G., H. Zhang, and P. J. Jonkier, 1995: Microphysical and turbulent structure of nocturnal stratocumulus as observed during ASTEX. *J. Atmos. Sci.*, **52**, 2763–2777.
- Ebert, E. E., and J. A. Curry, 1992: A parameterization of ice-cloud optical properties for climate models. *J. Geophys. Res.*, **97**, 3831–3836.
- Feingold, G., W. R. Cotton, S. M. Kreidenweis, and J. T. Davis, 1999: Impact of giant cloud condensation nuclei on drizzle formation in marine stratocumulus: Implications for cloud radiative properties. *J. Atmos. Sci.*, **56**, 4100–4117.
- , W. L. Eberhard, D. E. Veron, and M. Prevedì, 2003: First measurements of the Twomey indirect effect using ground-based remote sensors. *Geophys. Res. Lett.*, **30**, 1287, doi:10.1029/2002GL016633.
- Ferrier, B. S., 1994: A double-moment multiple-phase four-class bulk ice scheme. Part I: Description. *J. Atmos. Sci.*, **51**, 249–280.
- Fletcher, N. H., 1962: *The Physics of Rainclouds*. Cambridge University Press, 386 pp.
- Ghan, S. J., L. R. Leung, and R. C. Easter, 1997: Prediction of cloud droplet number in a general circulation model. *J. Geophys. Res.*, **102**, 21 777–21 794.
- Ghan, S., R. Easter, E. C. H. Abdul-Razzak, Y. Zhang, L. Leung, N. Laulainen, R. Saylor, and R. Zaveri, 2001: A physically-based estimate of radiative forcing by anthropogenic sulfate aerosol. *J. Geophys. Res.*, **106**, 5279–5293.
- Girard, E., and J. A. Curry, 2001: Simulation of Arctic low-level clouds observed during the FIRE Arctic Clouds Experiment using a new bulk microphysics scheme. *J. Geophys. Res.*, **106**, 15 139–15 154.
- Grell, G. A., J. Dudhia, and D. R. Stauffer, 1994: A description of the Fifth-Generation Penn State/NCAR Mesoscale Model (MM5). NCAR Tech. Note NCAR/TN-398 + STR, 138 pp.
- Hallet, J., and S. C. Mossop, 1974: Production of secondary ice particles during the riming process. *Nature*, **249**, 26–28.
- Han, Y., and E. R. Westwater, 1995: Remote sensing of tropospheric water and cloud liquid water by integrated ground-based sensors. *J. Atmos. Oceanic Technol.*, **12**, 1050–1059.
- Harrington, J. Y., M. P. Meyers, R. L. Walko, and W. R. Cotton, 1995: Parameterization of ice crystal conversion process due to vapor deposition for mesoscale models using double-moment basis functions. Part I: Basic formulation and parcel model results. *J. Atmos. Sci.*, **52**, 4344–4366.
- Herman, G. F., and J. A. Curry, 1984: Observational and theoretical studies of solar radiation in arctic stratus clouds. *J. Climate Appl. Meteor.*, **23**, 5–24.

- Hobbs, P. V., and A. L. Rangno, 1985: Ice particle concentrations in clouds. *J. Atmos. Sci.*, **42**, 2523–2549.
- , and —, 1998: Microstructures of low and middle-level clouds over the Beaufort Sea. *Quart. J. Roy. Meteor. Soc.*, **124**, 2035–2071.
- Intrieri, J. M., M. D. Shupe, T. Uttal, and B. J. McCarty, 2002: An annual cycle of Arctic cloud characteristics observed by radar and lidar at SHEBA. *J. Geophys. Res.*, **107**, 8030, doi:10.1029/2000JC000423.
- Janjic, Z. I., 1994: The step-mountain Eta coordinate model: Further developments of the convection, viscous layer, and turbulence closure schemes. *Mon. Wea. Rev.*, **122**, 927–945.
- Jayaweera, K. O. L. F., and T. Ohtake, 1973: Concentrations of ice crystals in arctic stratus clouds. *J. Res. Atmos.*, **7**, 199–207.
- Jensen, E. J., and L. Pfister, 2004: Transport and freeze-drying in the tropical tropopause layer. *J. Geophys. Res.*, **109**, D02207, doi:10.1029/2003JD004022.
- , and Coauthors, 1998: Ice nucleation processes in upper-tropospheric wave clouds during SUCCESS. *Geophys. Res. Lett.*, **25**, 1363–1366.
- , L. Pfister, T. Bui, A. Weinheimer, E. Weinstock, J. Smith, J. Pittman, and D. Baumgardner, 2005: Formation of a tropopause cirrus layer observed over Florida during CRYSTAL-FACE. *J. Geophys. Res.*, **110**, D03208, doi:10.1029/2004JD004671.
- Jiang, H., W. R. Cotton, J. O. Pinto, J. A. Curry, and M. J. Weisbluth, 2000: Cloud resolving simulations of mixed-phase arctic stratus observed during BASE: Sensitivity to concentration of ice crystals and large-scale heat and moisture advection. *J. Atmos. Sci.*, **57**, 2105–2117.
- Kalnay, E., and Coauthors, 1996: The NCEP–NCAR Reanalysis Project. *Bull. Amer. Meteor. Soc.*, **77**, 437–471.
- Key, J., 2001: *The Cloud and Surface Parameter Retrieval (CASPR) System for Polar AVHRR Data User's Guide*. Space Science and Engineering Center, University of Wisconsin, Madison, WI, 62 pp.
- , A. J. Schweiger, and R. S. Stone, 1997: Expected uncertainty in satellite-derived estimates of the high-latitude surface radiation budget. *J. Geophys. Res.*, **102**, 15 837–15 847.
- Khvorostyanov, V. I., and G. R. Toyan, 1988: Mathematical model of a three-layer orographic cloud system and its modification by ground-based generators. *Sov. Meteor. Hydrol.*, **1**, 34–47. (Translated by Allerton Press.)
- , and A. M. Yudov, 1988: Enhancement and redistribution of precipitation after seeding of wintertime frontal stratiform clouds. *Sov. Meteor. Hydrol.*, **7**, 16–28. (Translated by Allerton Press.)
- , and K. Sassen, 1998: Cirrus cloud simulation using explicit cloud microphysics and radiation. Part I: Model description. *J. Atmos. Sci.*, **55**, 1808–1821.
- , and J. A. Curry, 1999a: A simple analytical model of aerosol properties with account for hygroscopic growth, Part 1. Equilibrium size spectra and CCN activity spectra. *J. Geophys. Res.*, **104**, 2163–2174.
- , and —, 1999b: Towards the theory of stochastic condensation in clouds. Part II: Analytical solutions of the gamma distribution type. *J. Atmos. Sci.*, **56**, 3997–4013.
- , and —, 2000: A new theory of heterogeneous ice nucleation for application in cloud and climate models. *Geophys. Res. Lett.*, **27**, 4081–4084.
- , and —, 2005: The theory of ice nucleation by heterogeneous freezing of deliquescent mixed CCN. Part II: Parcel model simulation. *J. Atmos. Sci.*, **62**, 261–285.
- , —, I. Gultepe, and K. Strawbridge, 2003: A springtime cloud over the Beaufort Sea polynya: 3D simulation with explicit spectral microphysics and comparison with observations. *J. Geophys. Res.*, **108**, 4296, doi:10.1029/2001JD001489.
- , H. Morrison, J. A. Curry, D. Baumgardner, and P. Lawson, 2005: High ice supersaturation and modes of ice nucleation in thin tropopause cirrus: Simulation of the 13 July CRYSTAL case. *J. Geophys. Res.*, in press.
- Kong, F.-Y., and M. K. Yau, 1997: An explicit approach to microphysics in MC2. *Atmos.–Ocean*, **35**, 257–291.
- Korolev, A., G. A. Isaac, S. G. Cober, J. W. Strapp, and J. Hallett, 2003: Microphysical characterization of mixed-phase clouds. *Quart. J. Roy. Meteor. Soc.*, **129**, 39–65.
- Lawson, R. P., 2003: Continued quality-control and analysis of aircraft microphysical measurements. Final Rep., NASA FIRE, ACE LaRC PO L-14, 363 pp.
- , B. A. Baker, C. G. Schmitt, and T. L. Jensen, 2001: An overview of microphysical properties of Arctic clouds observed in May and July during FIRE ACE. *J. Geophys. Res.*, **106**, 14 989–15 014.
- Levkov, L., B. Rockel, H. Kapitzka, and E. Raschke, 1992: 3D mesoscale numerical studies of cirrus and stratus clouds by their time and space evolution. *Beitr. Phys. Atmos.*, **65**, 35–58.
- Liebe, H. J., G. A. Hufford, and T. Manabe, 1991: A model for the complex permittivity of water at frequencies below 1 thz. *Int. J. Infrared Millimeter Waves*, **12**, 659–675.
- Lin, Y.-L., R. D. Farley, and H. D. Orville, 1983: Bulk parameterization of the snow field in a cloud model. *J. Appl. Meteor.*, **22**, 1065–1089.
- Lohmann, U., 2002a: Possible aerosol effects on ice clouds via contact nucleation. *J. Atmos. Sci.*, **59**, 647–656.
- , 2002b: A glaciation indirect effect caused by soot aerosols. *Geophys. Res. Lett.*, **29**, 1052, doi:10.1029/2001GL014357.
- , J. Humble, W. R. Leaitch, G. A. Isaac, and I. Gultepe, 2001: Simulation of ice clouds during FIRE ACE using the CCCMA single-column model. *J. Geophys. Res.*, **106**, 15 123–15 138.
- , J. Zhang, and J. Pi, 2003: Sensitivity study of the effect of increased aerosol concentrations and snow crystal shapes on the snowfall rate in the Arctic. *J. Geophys. Res.*, **108**, 4341, doi:10.1029/2003JD003377.
- Maslanik, J. A., J. Key, C. W. Fowler, T. Nguyen, and X. Wang, 2001: Spatial and temporal variability of satellite-derived cloud and surface characteristics during FIRE-ACE. *J. Geophys. Res.*, **106**, 15 233–15 249.
- Meyers, M. P., P. J. DeMott, and W. R. Cotton, 1992: New primary ice nucleation parameterization in an explicit model. *J. Appl. Meteor.*, **31**, 708–721.
- , R. L. Walko, J. Y. Harrington, and W. R. Cotton, 1997: New RAMS cloud microphysics parameterization. Part II: The two-moment scheme. *Atmos. Res.*, **45**, 3–39.
- Miloshevich, L. M., H. Voemel, A. Paukkunen, A. J. Heymsfield, and S. J. Oltmanns, 2001: Characterization and correction of relative humidity measurements from Väisälä RS80-A radiosondes at cold temperatures. *J. Atmos. Oceanic Technol.*, **18**, 135–156.
- , M. D. Shupe, and J. A. Curry, 2003: Modeling clouds observed at SHEBA using a bulk parameterization imple-

- mented into a single-column model. *J. Geophys. Res.*, **108**, 4255, doi:10.1029/2002JD002229.
- , J. A. Curry, and V. I. Khvorostyanov, 2005a: A new double-moment microphysics scheme for application in cloud and climate models. Part I: Description. *J. Atmos. Sci.*, **62**, 1665–1677.
- , —, M. D. Shupe, and P. Zuidema, 2005b: A new double-moment microphysics scheme for application in cloud and climate models. Part II: Single-column modeling of arctic clouds. *J. Atmos. Sci.*, **62**, 1678–1693.
- Nicholls, S., 1984: The dynamics of stratocumulus: Aircraft observations and comparison with a mixed layer model. *Quart. J. Roy. Meteor. Soc.*, **110**, 783–820.
- Persson, P. O. G., C. W. Fairall, E. L. Andreas, P. S. Guest, and D. K. Perovich, 2002: Measurements near the Atmospheric Surface Flux Group tower at SHEBA: Near-surface conditions and surface energy budget. *J. Geophys. Res.*, **107**, 8045, doi:10.1029/2000JC000705.
- Pinto, J. O., 1998: Autumnal mixed-phase cloudy boundary layers in the Arctic. *J. Atmos. Sci.*, **55**, 2016–2038.
- , and J. A. Curry, 1995: Atmospheric convective plumes emanating from leads. 2. Microphysical and radiative processes. *J. Geophys. Res.*, **100**, 4633–4642.
- , —, and J. M. Intrieri, 2001: Cloud-aerosol interactions during autumn over Beaufort Sea. *J. Geophys. Res.*, **106**, 15 077–15 097.
- Pruppacher, H. R., and J. D. Klett, 1997: *Microphysics of Clouds and Precipitation*. Kluwer Academic, 954 pp.
- Radke, L. F., J. F. Lyons, D. A. Hegg, and P. V. Hobbs, 1984: Airborne observations of arctic aerosols. Characterizations of arctic haze. *Geophys. Res. Lett.*, **11**, 393–396.
- Rangno, A. L., and P. V. Hobbs, 2001: Ice particles in stratiform clouds in the Arctic and possible mechanisms for the production of high ice particle concentrations. *J. Geophys. Res.*, **106**, 15 065–15 075.
- Rauber, R. M., and A. Tokay, 1991: An explanation for the existence of supercooled water at the top of cold clouds. *J. Atmos. Sci.*, **48**, 1005–1023.
- Reisner, J., R. M. Rasmussen, and R. T. Bruintjes, 1998: Explicit forecasting of supercooled liquid water in winter storms using the MM5 forecast model. *Quart. J. Roy. Meteor. Soc.*, **124**, 1071–1107.
- Rogers, D. C., 1982: Field and laboratory studies of ice nucleation in winter orographic clouds. Ph.D. dissertation, University of Wyoming, 161 pp.
- , P. J. DeMott, and S. M. Kreidenweis, 2001: Airborne measurements of tropospheric ice-nucleating aerosol particles in the Arctic spring. *J. Geophys. Res.*, **106**, 15 053–15 063.
- Rogers, R. R., and M. K. Yau, 1989: *A Short Course in Cloud Physics*. 3rd ed. Pergamon Press, 293 pp.
- Rosenkranz, P. W., 1998: Water vapor microwave continuum absorption: A comparison of measurements and models. *Radio Sci.*, **33**, 919–928.
- Rotstain, L. D., and J. E. Penner, 2001: Indirect aerosol forcing, quasi forcing, and climate response. *J. Climate*, **14**, 2960–2975.
- Rutledge, S. A., and P. V. Hobbs, 1984: The mesoscale and microscale structure and organization of clouds and precipitation in mid-latitude cyclones. Part XII: A diagnostic modeling study of precipitation development in narrow cold-frontal rainbands. *J. Atmos. Sci.*, **41**, 2949–2972.
- Sassen, K., and G. C. Dodd, 1989: Haze particle nucleation simulation in cirrus clouds, and application for numerical and lidar studies. *J. Atmos. Sci.*, **46**, 3005–3014.
- Shupe, M. D., and J. M. Intrieri, 2004: Cloud radiative forcing of the Arctic surface: The influence of cloud properties, surface albedo, and solar zenith angle. *J. Climate*, **17**, 616–628.
- , T. Uttal, S. Y. Matrasov, and A. S. Frisch, 2001: Cloud water contents and hydrometeor sizes during the FIRE Arctic Clouds Experiment. *J. Geophys. Res.*, **106**, 15 015–15 028.
- Slingo, A., 1989: A GCM parameterization for the shortwave optical properties of water clouds. *J. Atmos. Sci.*, **46**, 1419–1427.
- Slinn, W. G. N., and J. M. Hales, 1971: A reevaluation of the role of thermophoresis as a mechanism of in- and below-cloud scavenging. *J. Atmos. Sci.*, **28**, 1465–1471.
- Stevens, B., G. Feingold, W. R. Cotton, and R. L. Walko, 1996: Elements of the microphysical structure of numerically simulated nonprecipitating stratocumulus. *J. Atmos. Sci.*, **53**, 980–1006.
- Stull, R. B., 1988: *An Introduction to Boundary-Layer Meteorology*. Kluwer Academic Press, 666 pp.
- Turner, D. D., B. M. Lesht, S. A. Clough, J. C. Liljegren, H. E. Revercomb, and D. C. Tobin, 2003: Dry bias and variability in Väisälä RS80-H radiosondes: The ARM Experience. *J. Atmos. Oceanic Technol.*, **20**, 117–132.
- Twomey, S., 1959: The nuclei of natural cloud formation, II, The supersaturation in natural clouds and the variation of cloud droplet concentration. *Geophys. Pura Appl.*, **43**, 243–249.
- , 1977: The influence of pollution on the shortwave albedo of clouds. *J. Atmos. Sci.*, **34**, 1149–1152.
- Uttal, T., and Coauthors, 2002: The Surface Heat Budget of the Arctic Ocean. *Bull. Amer. Meteor. Soc.*, **83**, 255–275.
- Vali, G., 1974: Contact ice nucleation by natural and artificial aerosols. *Conf. Cloud Physics*, Tucson, AZ, Amer. Meteor. Soc., 34–37.
- Walko, R., W. R. Cotton, M. P. Meyers, and J. Y. Harrington, 1995: New RAMS cloud microphysics parameterization. Part I: The single-moment scheme. *Atmos. Res.*, **38**, 29–62.
- Wang, J., H. Cole, D. J. Carlson, E. R. Miller, K. Beierle, A. Paunkunen, and T. K. Lane, 2002: Corrections of humidity measurement errors from the Väisälä RS80 radiosonde—Application to TOGA COARE data. *J. Atmos. Oceanic Technol.*, **19**, 981–1002.
- Westwater, E. R., Y. Han, M. D. Shupe, and S. Y. Matrasov, 2001: Analysis of integrated cloud liquid water and precipitable water vapor retrievals from microwave radiometer during SHEBA. *J. Geophys. Res.*, **106**, 32 019–32 030.
- Wylie, D., 2001: Arctic weather during FIRE ACE. *J. Geophys. Res.*, **106**, 15 363–15 375.
- Young, K. C., 1974: The role of contact nucleation in ice phase initiation in clouds. *J. Atmos. Sci.*, **31**, 768–780.
- Yum, S. S., and J. G. Hudson, 2001: Vertical distribution of cloud condensation nuclei spectra over the springtime Arctic Ocean. *J. Geophys. Res.*, **106**, 15 045–15 052.
- Zuidema, P., and Coauthors, 2005: An arctic springtime mixed-phase cloud boundary layer observed during SHEBA. *J. Atmos. Sci.*, **62**, 160–176.